

A receding-horizon multi-contact motion planner for legged robots in challenging environments

D.S.J. Derwent^a, S. Watson^a, B.V. Adorno^{a,*}

^aManchester Centre for Robotics and AI, University of Manchester, Oxford Rd, Manchester M13 9PL, UK

Abstract

We present a novel receding-horizon multi-contact motion planner for legged robots in challenging scenarios, able to plan motions such as chimney climbing, navigating very narrow passages or crossing large gaps. Our approach adds new capabilities to the state of the art, including the ability to reactively re-plan in response to new information, and planning contact locations and whole-body trajectories simultaneously, simplifying the implementation and removing the need for post-processing or complex multi-stage approaches. Our method is more resistant to local minima problems than other potential field based approaches, and our quadratic-program-based posture generator returns nodes more quickly than those of existing algorithms. Rigorous statistical analysis shows that, with short planning horizons (*e.g.*, one step ahead), our planner is faster than the state-of-the-art across all scenarios tested (between 45% and 98% faster on average, depending on the scenario), while planning less efficient motions (requiring 5% fewer to 700% more stance changes on average). In all but one scenario (Chimney Walking), longer planning horizons (*e.g.*, four steps ahead) extended the average planning times (between 73% faster and 400% slower than the state-of-the-art) but resulted in higher quality motion plans (between 8% more and 47% fewer stance changes than the state-of-the-art).

Keywords: Motion Planning, Legged Robots, Hexapods, Vector-Field Inequalities, Dual Quaternion Algebra

1. Introduction

A unique challenge of legged motion planning is the need to plan how the robot will make and break contacts with its environment. If the desired form of motion is known and approximately cyclical (*e.g.*, walking across moderately uneven terrain), it may suffice to use a pre-specified or adaptive gait. However, if robots are to perform acyclic motions such as navigating sparse irregular footholds [1] or rough terrain where the precise contact locations are critical [2], then they must explicitly plan where, and in what sequence, individual contacts should be made or broken. This is referred to as multi-contact motion planning.

Since fully enumerating the set of all possible contact combinations (referred to as *stances* [1]) is usually impractical, many multi-contact planners use a tree-search method to construct an approximate map of the stance space, which is then searched to generate the motion plan [1, 3, 4, 5]. The design of the search process has significant ramifications for the behaviour of the overall planning algorithm, and often involves trade-offs between the generality of the planner, the time needed to plan, and the quality of planning outputs [6].

Additionally, to ensure that a given stance is feasible, multi-contact planners must find a safe whole-body configuration that allows the robot to realise the intended stance while respecting certain constraints (*e.g.*, avoiding collisions, maintaining balance, *etc.*). The robot must also be able to safely transition into the intended stance from a previous stance, meaning that a safe whole-body trajectory linking the two stances must also be found. These lower-level elements of planning are often handled by a dedicated ‘posture generator’, which finds *transition configurations* through a numerical optimisation process [4, 5].

1.1. Related Works

Multi-contact planners are typically divided into Motion-Before-Contact (MBC) and Contact-Before-Motion (CBM) approaches [1]. MBC algorithms plan a collision-free torso trajectory and then use a posture generator to find stances and transition configurations that enable each resulting torso pose. For example, the planner of Tonneau *et al.* generates a large offline dataset of randomly sampled limb configurations that is searched at runtime to assemble configurations [6]. MBC planners typically execute faster than CBM planners, needing only to consider the robot’s torso pose rather than the full configuration. However, MBC approaches must assume what kinds of motion the robot can execute and constrain the trajectory search to regions where such motions are most likely possible, leading to a

*Corresponding author

Email addresses: daniel.johnson-2@manchester.ac.uk
(D.S.J. Derwent), simon.watson@manchester.ac.uk (S. Watson),
bruno.adorno@manchester.ac.uk (B.V. Adorno)

loss of generality (*e.g.*, [6] does not consider configurations where all contacts are on vertical surfaces).

Alternatively, CBM algorithms plan a series of stances that are combined to form an overall motion, using the posture generator to verify their feasibility. Early CBM planners by Bretl *et al.*, explicitly enumerated all available stances, and used a posture generator based on random sampling to verify the connectivity of the stance graph [1, 2, 7]. These approaches assume that only a small set of discrete footholds is available to the robot, and thus all stance combinations can be considered. However, if the planner must identify footholds autonomously on continuous surfaces, then this kind of explicit enumeration becomes impractical.

Another approach by Mordatch *et al.* uses numerical optimisation to simultaneously plan whole body motions and supporting contacts, but again this approach relies on a pre-surveyed list of candidate footholds, rather than identifying footholds autonomously [8].

The Contacts Very-Best First Planning (CVBFP) algorithm [4] improves upon these approaches with a search process that plans contacts between a given contact patch \mathcal{P} (attached to the robot) and contact area \mathcal{A} (attached to the environment) without specifying the location of \mathcal{P} on \mathcal{A} . Instead, the posture generator chooses the optimal contact location on \mathcal{A} by minimising a potential field, returning a transition configuration that forms the optimal contact [4]. However, CVBFP assumes that safe whole-body trajectories between neighbouring transition configurations exist without verifying this to be the case.

This is partially addressed by the multi-stage framework presented in [5], wherein the first stage uses a Rapidly-exploring Random Tree method to compute a sequence of stances and transition configurations, and the second stage generates a whole body trajectory that executes the sequence. However, because the stance sequence is planned prior to the trajectory, it remains possible that a stance sequence may be returned for which a feasible trajectory cannot be found.

It is notable that all of the approaches discussed are *global* planning methods, meaning that they return a complete plan from the initial state to the goal state [1, 8, 4, 5]. Global approaches can often generate direct and efficient overall motion plans, but they also typically require more time to plan than local approaches, since planning the whole motion is generally more costly than planning only the next few steps. Global approaches are also less able to update their plans in response to gaining new information about the environment and instead may need to repeat the entire planning process from scratch.

Local planning methods for legged robots typically focus on walking over uneven terrains. For example, the technique in [9] uses imitation learning to identify desirable footholds and plans the torso trajectory over the next four steps. Likewise, in [10], whole-body trajectories are optimised over the next step cycle to achieve intermediate planning goals that combine to form the complete task.

Alternatively, Melon *et al.* [11] proposes a receding horizon implementation of the popular Trajectory Optimisation for Walking Robots (TOWR) framework [12], using a mix of heuristic methods and imitation learning to find effective hot-start conditions for TOWR to execute at online rates.

While these approaches are able to plan multi-contact motions in real time and update these plans easily, they lack the generality and formal safety guarantees offered by conventional CBM approaches.

1.2. Statement of Contributions

We propose a novel multi-contact motion planning framework, including a receding-horizon tree-search algorithm and a posture generator based on vector-field inequalities. The proposed framework retains the generality of other CBM approaches, while also improving upon the state-of-the-art by:

- Rapidly re-planning in response to new information.
- Improving robustness to planning problems caused by local minima in the potential field.
- Guaranteeing that kinematically feasible whole-body trajectories between stances exist *before* they are added to the search tree, verifying assumptions made in [5, 4].
- Generating the stance, transition configuration, and whole-body trajectory *simultaneously*, removing the need for any additional stages of planning.
- Improving execution times without compromising on generality.

We demonstrate our approach by planning several challenging motions for the Corin hexapod [13], including scenarios where some or all of the robot’s contacts are on vertical surfaces (see Section 8 for details). Finally, we use Bayesian data analysis techniques to rigorously compare our planner’s performance to that of CVBFP [4].

This work is an extension of previous work presented at TAROS 2025 [14], which focussed on our posture generator only. This work discusses the complete planning framework, composed of both the search process *and* the posture generator, to offer a fuller picture of the planning process. We also present new results from experiments and data analysis conducted after the publication of [14] that include new insights into the behaviour of the motion planner.

1.3. Paper Organisation

The remainder of the paper is organised as follows. Section 2 provides some preliminary information regarding the mathematical notations and terminology used throughout the paper. Section 3 presents a high-level overview of our proposed planning algorithm and its main components.

Section 4 details the guide path and potential field that are used to guide both the tree search and the posture generation process. Section 5 discusses our novel posture generation approach, beginning with a high-level introduction and going on to derive the relevant constraints and objective functions. Section 6 describes local minima problems that affect CBM planners and mitigation strategies. Section 7 covers the numerical integration method used to update the configuration model during posture generation and contact drift correction. Section 8 discusses the simulation experiments performed with the planner in several different scenarios including a thorough statistical comparison against the state-of-the-art. Finally, Section 9 concludes the paper and presents some future work.

2. Preliminaries

This section introduces the concepts from dual quaternion algebra that are used for robot modelling and control throughout this work and defines several terms and symbols used in later sections.

2.1. Dual Quaternion Algebra

The planning framework we present relies heavily on geometrical primitives, such as planes, lines, and points, in addition to rigid transformations, twists, and wrenches, all of which are elegantly represented using dual quaternion algebra. Additionally, several robot modelling and control techniques that are particularly useful for solving posture generation problems have been developed that utilise the strong algebraic properties of dual quaternion algebra, making this an attractive choice.

Quaternions belong to the set $\mathbb{H} \triangleq \{h_1 + \hat{i}h_2 + \hat{j}h_3 + \hat{k}h_4 : h_1, h_2, h_3, h_4 \in \mathbb{R}\}$, where \hat{i} , \hat{j} , and \hat{k} denote imaginary units such that $\hat{i}^2 = \hat{j}^2 = \hat{k}^2 = \hat{i}\hat{j}\hat{k} = -1$. Quaternions can represent 3D orientations and rotations using elements of the subset $\mathbb{S}^3 \triangleq \{\mathbf{h} \in \mathbb{H} : \|\mathbf{h}\| = 1\}$, as well as positions using elements of the subset $\mathbb{H}_p \triangleq \{\mathbf{h} \in \mathbb{H} : \text{Re}(\mathbf{h}) = 0\}$ [15]. *Dual* quaternions extend quaternions and belong to the set $\mathcal{H} \triangleq \{\mathbf{h} + \varepsilon\mathbf{h}' : \mathbf{h}, \mathbf{h}' \in \mathbb{H}, \varepsilon^2 = 0, \varepsilon \neq 0\}$. The set of *unit* dual quaternions, $\mathcal{S} \triangleq \{\mathbf{h} \in \mathcal{H} : \|\mathbf{h}\| = 1\}$, represent rigid transformations in 3D space, and any $\underline{\mathbf{x}} \in \mathcal{S}$ can be written as $\underline{\mathbf{x}} = \mathbf{r} + \varepsilon \frac{1}{2} \mathbf{p} \mathbf{r}$, where $\mathbf{r} \in \mathbb{S}^3$ and $\mathbf{p} \in \mathbb{H}_p$ denote the rotation and translation components of the rigid transformation respectively [15]. Analogously to \mathbb{H}_p , we also define the subset $\mathcal{H}_p \triangleq \{\mathbf{h} + \varepsilon\mathbf{h}' : \mathbf{h}, \mathbf{h}' \in \mathbb{H}_p\}$, which is useful for modelling certain primitives.

The coefficients of elements of any of the aforementioned sets can be bijectively mapped into vectors. For example,

$$\begin{aligned} \text{vec}_3(h_1 + \hat{i}h_2 + \hat{j}h_3) &= [h_1 \ h_2 \ h_3]^T \\ \text{vec}_4(h_1 + \hat{i}h_2 + \hat{j}h_3 + \hat{k}h_4) &= [h_1 \ h_2 \ h_3 \ h_4]^T. \end{aligned} \quad (1)$$

This property is very useful for performing numerical optimisation, discussed in more detail in Section 2.3.

2.2. Terminology

The *workspace* is written as $\mathcal{W} \subset \mathbb{H}_p$, with its fixed coordinate frame denoted $\mathcal{F}_{\mathcal{W}}$. The region of \mathcal{W} occupied by obstacles that the robot cannot intersect (*the obstacle region*) is represented by $\mathcal{O} \subset \mathcal{W}$.

In this work, *configurations* are represented in the form $\mathbf{q} = [\text{vec}_4(\mathbf{r})^T \ \text{vec}_3(\mathbf{p})^T \ \boldsymbol{\theta}^T]^T \in \mathbb{R}^n$ such that the robot's pose is given by the unit dual quaternion $\underline{\mathbf{x}} = \mathbf{r} + \varepsilon \frac{1}{2} \mathbf{p} \mathbf{r}$, the vector $\boldsymbol{\theta} \in \mathbb{R}^{n_{\theta}}$ represents the joint coordinates, and $n = n_{\theta} + 7$. Each joint may be either prismatic or revolute with a bounded range of motion. The set of all configurations is the configuration space \mathcal{Q} .

A contact area \mathcal{A} is a 2D surface in \mathcal{W} on which a contact may be formed. The set of all contact areas is denoted $\mathcal{E} \triangleq \{\mathcal{A}_1, \mathcal{A}_2, \dots, \mathcal{A}_{n_{\mathcal{E}}}\}$.

A contact patch \mathcal{P}_i is an area or point on the robot that is permitted to participate in contacts. For a humanoid robot, contact patches may include feet and hands, as well as knees, elbows, or other parts of the robot. For hexapods and quadrupeds, this is more likely to include only the robot's feet. The set of contact patches is denoted \mathcal{R} .

A contact $c_{i,j}$ between a contact patch $\mathcal{P}_i \in \mathcal{R}$ and a contact area $\mathcal{A}_j \in \mathcal{E}$ is denoted $c_{i,j} = (\mathcal{P}_i, \mathcal{A}_j, \mathbf{p}_j^{\mathcal{A}_j})$, where $\mathbf{p}_j^{\mathcal{A}_j} \in \mathcal{A}_j$ represent the position of the contact in the reference frame of area \mathcal{A}_j .

A *stance* s refers to a set of multiple contacts maintained simultaneously, written as $s \triangleq \{c_1, c_2, \dots, c_{n_s}\}$ [1]. The *stance space* is the set of all stances, denoted \mathcal{S} . The set of configurations that satisfy a given stance s is written as $\mathcal{Q}_s \subset \mathcal{Q}$.

A configuration is said to be *feasible* if it respects the constraints on the robot (*e.g.*, collision avoidance, maintaining quasi-static balance, maintaining contacts, kinematic constraints, *etc.*). The set of all feasible configurations is written as $\mathcal{F} \subset \mathcal{Q}$. Different constraints are associated with different stances (*e.g.*, which configurations are balanced depends on the stance), and as such it is often useful to consider $\mathcal{F}_s \subset \mathcal{Q}_s$, the set of all feasible configurations in stance s . Stance s is said to be feasible if $\mathcal{F}_s \neq \emptyset$.

If two neighbouring stances s_1 and s_2 are linked by a configuration $\mathbf{q}_t \in \mathcal{F}_{s_1} \cap \mathcal{F}_{s_2}$, then \mathbf{q}_t is said to be a *transition configuration* between s_1 and s_2 .

2.3. Vector-Field Inequalities

Using dual quaternion algebra, one can straightforwardly formulate task-space constrained controllers with geometrical constraints in the form of quadratic programs with linear constraints in the control inputs. As constrained controllers based on vector-field inequalities play a crucial role in our multi-contact motion planner, let us briefly recapitulate their basic formulation. Given a task vector $\mathbf{x} \triangleq \mathbf{x}(\mathbf{q}) \in \mathbb{R}^m$, which might represent, for instance, the robot pose, position, or orientation, and a constant desired task vector $\mathbf{x}_d \in \mathbb{R}^m$, we can minimise the

error vector $\tilde{\mathbf{x}} \triangleq \mathbf{x} - \mathbf{x}_d$ using the control law

$$\begin{aligned} \mathbf{u} \in \operatorname{argmin}_{\dot{\mathbf{q}}} \quad & \|\mathbf{J}_{\tilde{\mathbf{x}}}\dot{\mathbf{q}} + \eta_o \tilde{\mathbf{x}}\|_2^2 + \lambda^2 \|\dot{\mathbf{q}}\|_2^2 \\ \text{subject to} \quad & \mathbf{W}_1(\mathbf{q})\dot{\mathbf{q}} \preceq \mathbf{w}_1(\mathbf{q}) \\ & \mathbf{W}_2(\mathbf{q})\dot{\mathbf{q}} = \mathbf{w}_2(\mathbf{q}), \end{aligned} \quad (2)$$

where $\mathbf{J}_{\tilde{\mathbf{x}}} \triangleq \mathbf{J}_{\tilde{\mathbf{x}}}(\mathbf{q}) = \partial \tilde{\mathbf{x}} / \partial \mathbf{q}$, $\eta_o \in (0, \infty)$ and $\lambda \in (0, \infty)$. The matrix/vector pair $\mathbf{W}_1(\mathbf{q}) \in \mathbb{R}^{\ell_I \times n}$ and $\mathbf{w}_1(\mathbf{q}) \in \mathbb{R}^{\ell_I}$ impose ℓ_I linear *inequality* constraints on $\dot{\mathbf{q}}$, whereas $\mathbf{W}_2(\mathbf{q}) \in \mathbb{R}^{\ell_E \times n}$ and $\mathbf{w}_2(\mathbf{q}) \in \mathbb{R}^{\ell_E}$ impose ℓ_E linear *equality* constraints on $\dot{\mathbf{q}}$ [16].

The vector-field inequality (VFI) framework allows the transformation of non-linear geometric constraints on \mathbf{q} into linear constraints on $\dot{\mathbf{q}}$ that ensure that the original constraints on \mathbf{q} are met [16]. This requires only a differentiable signed distance function $d \triangleq d(\mathbf{q})$ between a geometrical entity kinematically coupled to the robot and another geometrical primitive in the task space, and the Jacobian matrix $\mathbf{J}_d \triangleq \mathbf{J}_d(\mathbf{q}) \in \mathbb{R}^{1 \times n}$ such that $\dot{d} = \mathbf{J}_d \dot{\mathbf{q}}$ [16].

To keep a robot entity outside of a given zone, *e.g.*, for collision avoidance, a signed distance $d(\mathbf{q})$ is defined between the robot body and the restricted zone and a minimum safe distance requirement $d(\mathbf{q}) \geq d_{\text{safe}}$, shown on the *left* in Figure 1, is imposed. By defining an error term $\tilde{d}(\mathbf{q}) \triangleq d(\mathbf{q}) - d_{\text{safe}}$ the requirement is rewritten as $\tilde{d}(\mathbf{q}) \geq 0$. Hence, using the VFI framework, this requirement is enforced using the constraint

$$\dot{\tilde{d}}(\mathbf{q}) \geq -\eta_d \tilde{d}(\mathbf{q}), \quad (3)$$

where $\eta_d \in (0, \infty)$ determines the maximum approach velocity of the robot body towards the restricted zone as a function of the distance to the minimum safe distance [16]. By applying Gronwall's Lemma, it can be shown that if the robot body lies outside of the restricted zone at time $t = 0$, meaning $\tilde{d} \geq 0$, then $\tilde{d}(\mathbf{q}) \geq 0$ for all times $t > 0$ [16].

Given that $\dot{d}_{\text{safe}} = 0$ for all t , then $\dot{\tilde{d}}(\mathbf{q}) = \mathbf{J}_d \dot{\mathbf{q}}$. Hence, (3) is rewritten as

$$-\mathbf{J}_d \dot{\mathbf{q}} \leq \eta_d \tilde{d}(\mathbf{q}). \quad (4)$$

Similarly, to keep a robot entity inside a given zone, *e.g.*, keeping the centre of mass inside a support region, the requirement is restated as $\tilde{d}(\mathbf{q}) \leq 0$ (shown on the *right* in Figure 1) to obtain the constraint

$$\dot{\tilde{d}}(\mathbf{q}) \leq -\eta_d \tilde{d}(\mathbf{q}) \iff \mathbf{J}_d \dot{\mathbf{q}} \leq -\eta_d \tilde{d}(\mathbf{q}). \quad (5)$$

Robot entities and zones of interest (*i.e.*, restricted zones and safe zones) can take on a wide variety of forms, with distance functions and corresponding Jacobians defined in the literature for combinations of points, lines, planes and many others [16, 17, 18].

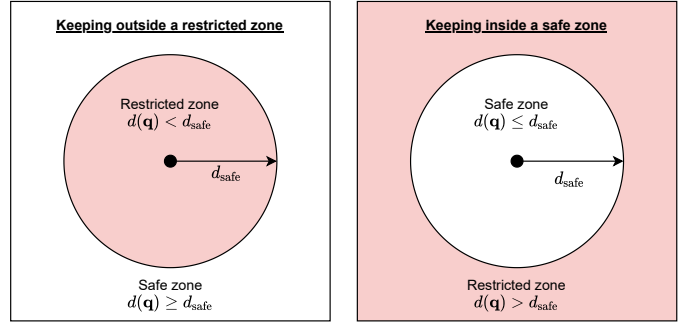


Figure 1: Illustrations of keeping the robot outside a restricted zone (*left*), in which case constraint (4) is applied, and inside a safe zone (*right*), in which case constraint (5) is applied.

3. An Overview of Receding Horizon Planning

This section offers a high level overview of our algorithm, focussing on the receding-horizon, breadth-first tree-search algorithm that improves upon the state-of-the-art by:

- Quickly re-planning in response to new information;
- Having only a single stage and a consistent policy for expanding nodes, which reduces the complexity of the implementation;
- Allowing the user to choose how much to prioritise performance versus quality of planning outputs by adjusting the horizon depth parameter κ_{max} .

3.1. Algorithm Description

As discussed in Section 1, many CBM algorithms are *global* planners, meaning that they generate a single, complete motion plan from the robot's starting state to its goal state [1, 8, 4, 5]. By contrast, given the robot's *current* state and the goal state, a *receding horizon planner* considers possible motions until a planning horizon is reached, at which point the most promising step from the current state is executed. This process repeats until the robot arrives at the goal state. The advantage of doing so is that the plan can be continuously adapted according to the best current information the robot has about the environment and its own state, providing reactivity and adaptability.

In this work, robot states are represented by nodes, written as $\mathbf{n}_i = (\mathbf{n}_{i-1}, s_i, \mathbf{q}_i, \mathcal{T}_{i-1,i})$, where $s_i \in \mathcal{S}$ and $\mathbf{q}_i \in \mathcal{F}_{s_i}$ denote the robot's stance and feasible configuration, whereas \mathbf{n}_{i-1} denotes the parent node of \mathbf{n}_i (*i.e.*, a previous state) and $\mathcal{T}_{i-1,i} \subset \mathcal{Q}$ denotes a feasible, whole-body, quasi-static, configuration space trajectory connecting node \mathbf{n}_{i-1} to node \mathbf{n}_i . Note that since the trajectory $\mathcal{T}_{i-1,i}$ is quasi-static, the reverse trajectory $\mathcal{T}_{i,i-1}$ can be obtained by reversing the order of the elements in $\mathcal{T}_{i-1,i}$.

A flowchart of the proposed Receding Horizon Contact Planning (RHCP) algorithm is given in Figure 2. First, a coarse global path is generated (shown in *red*) to guide the contact planning. Then, the main planning loop begins, with the initial node being re-designated as the root node

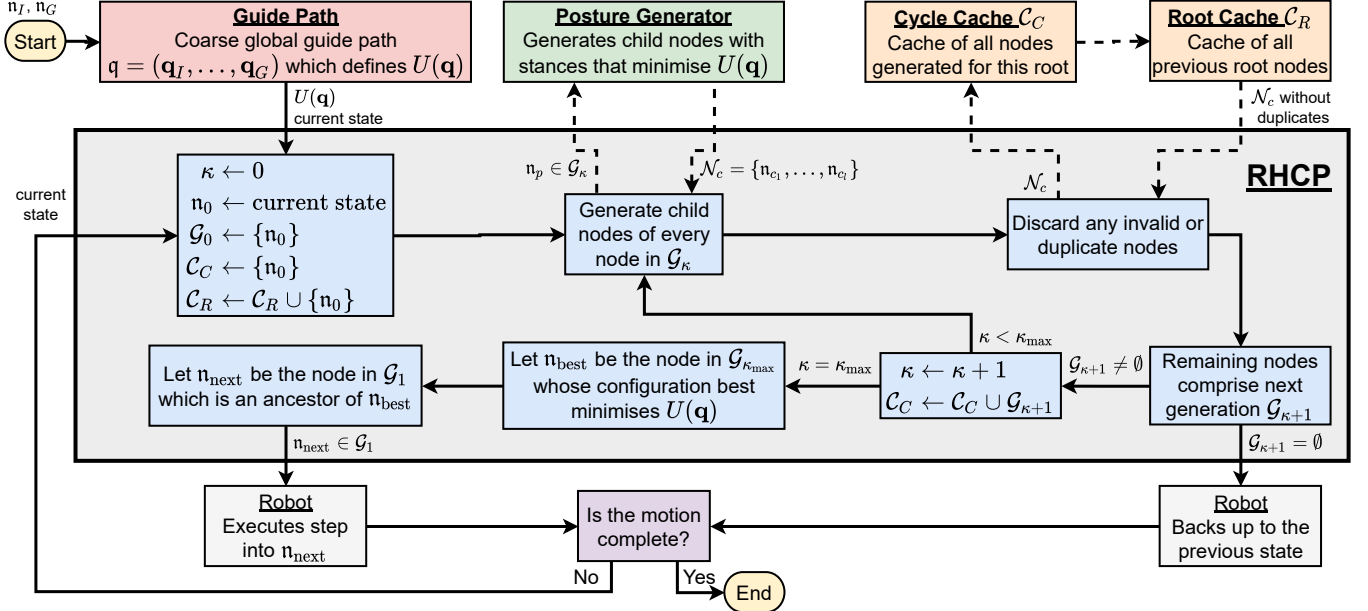


Figure 2: Flowchart illustrating the RHCP planning algorithm.

n_0 and the root generation¹ being defined as $G_0 = \{n_0\}$. The posture generator (shown in *green*) is then called to find the child nodes of n_0 , with each one representing a possible step that the robot could take. The cycle cache C_C and root cache C_R (shown in *orange*) are used to find and prune any duplicate nodes, and those that remain comprise the next generation G_1 . If the horizon has not been reached, then the current step κ is incremented and the posture generator is called again to populate the new generation G_2 . Once the horizon is reached (*i.e.*, $\kappa = \kappa_{max}$), the best node in generation $G_{\kappa_{max}}$ is found and the robot executes the step in G_1 that brings it towards this state. The process then repeats, with the resulting robot state becoming the new root node, until the goal is reached. The next subsections detail each of those mechanisms.

3.1.1. Potential Field Guide

The guide path is comprised of a sequence of waypoint configurations $q \triangleq (q_1, \dots, q_G)$, much like in [4], and the waypoint configurations may be provided by the user or generated autonomously [19]. Also like [4], a potential field $U : \mathcal{Q} \rightarrow [0, \infty)$ is defined based on q that incentivises the robot to move towards the goal state while keeping close to the guide path. The formulation of $U(q)$ is discussed further in Section 4.

3.1.2. Child Generation

The main planning loop begins by setting the generation count $\kappa \in \mathbb{N}_0$ to 0 and storing the current state in the

root node n_0 . It is assumed that all contact patches $\mathcal{P} \in \mathcal{R}$ are in contact in the root stance s_0 . The root generation G_0 , cycle cache C_C , and root cache C_R are also each defined at this stage as sets containing only n_0 . Every parent node $n_p \in G_0$ is then expanded (in this case only n_0), with the posture generator being called to generate the ℓ child nodes, each designated as $n_{c_k} = (n_{p_k}, s_{c_k}, q_{c_k}, \mathcal{T}_{p_k, c_k})$, $k \in \{1, \dots, \ell\}$.

One child node is specified for each contact patch-area pair $(\mathcal{P}_i, \mathcal{A}_j)$, each containing a stance s_{c_k} that differs from its parent stance s_{p_k} . The chosen contact patch \mathcal{P}_i is moved to the location on contact area \mathcal{A}_j that best minimises $U(q)$. All of the remaining contacts in s_{p_k} are maintained in s_{c_k} .

3.1.3. Pruning

Any invalid or duplicate child nodes are then rejected. A node is invalid if the posture generator fails to find a feasible configuration or linking trajectory (*e.g.*, the requested contact cannot be safely broken). A node is considered a duplicate if its stance s_c is too similar to that of any node in the cycle cache C_C or the root cache C_R . Two stances, s_1 and s_2 , are considered ‘too similar’ if, for every contact $c_i \in s_1$, there exists a contact $c_j \in s_2$ involving the same contact patch-area pair as in c_i such that the distance between c_i and c_j is below a user-defined threshold distance $d_{min} \in (0, \infty)$.

3.1.4. Completing the Cycle

The remaining valid, non-duplicate child nodes comprise the next generation G_1 and are added to the cycle cache C_C . If at least one such node is returned (*i.e.*, $G_1 \neq \emptyset$), then the generation count κ is incremented. If $\kappa < \kappa_{max}$, then the cycle repeats, this time expanding

¹Except for G_0 , which contains only the root node, the κ th generation, G_κ , is written as a set of nodes that contains all valid, non-duplicate child nodes of all nodes in the generation $G_{\kappa-1}$.

3.2 Analysis

6

every node in \mathcal{G}_1 , producing the next generation \mathcal{G}_2 , and so on until $\mathcal{G}_{\kappa_{\max}}$.

Once $\kappa = \kappa_{\max}$, the node in the final generation $\mathcal{G}_{\kappa_{\max}}$ that best minimises the potential field $U(\mathbf{q})$ is identified, designated \mathbf{n}_{best} . A backward search is conducted to find the node in \mathcal{G}_1 from which \mathbf{n}_{best} descends, designated \mathbf{n}_{next} , and the motion connecting \mathbf{n}_0 to \mathbf{n}_{next} is executed by the robot.

If this motion brings the robot into the goal state, then the planning concludes. If not, the planner is called again to determine the *next* step to take, with the current robot state becoming the new root node and being added to the root cache \mathcal{C}_R , preventing it from being generated again in future cycles.

3.1.5. Retreating

If no valid, non-duplicate child nodes remain to populate a generation $\mathcal{G}_{\kappa+1}$, then the robot returns to its previous state (*i.e.*, the parent node of \mathbf{n}_0) because all descendants of \mathbf{n}_0 will eventually lead to a dead end at the κ th step (*i.e.*, there are no valid stances after \mathcal{G}_κ). The planning cycle then repeats, as depicted in Figure 2, in order to identify the *next-best* line of exploration. Since this time \mathbf{n}_0 is already in the root cache \mathcal{C}_R , it is considered a duplicate and is excluded from \mathcal{G}_1 . The planner is thus prevented from returning to previously occupied root nodes that are known to be ‘dead ends’.

If the robot is instructed to retreat while in its initial state, when there is no previous state to retreat to, then the planning is considered to have failed, and no route is returned.

3.2. Analysis

The maximum number of posture generator calls per cycle is

$$n_{\max} = \sum_{\kappa=1}^{\kappa_{\max}} (n_{\mathcal{R}} n_{\mathcal{E}})^\kappa, \quad (6)$$

where $n_{\mathcal{R}}, n_{\mathcal{E}} \in \mathbb{N}$ denote the number of contact patches in \mathcal{R} and the number of contact areas in \mathcal{E} , respectively. It is clear from (6) that the maximum number of calls increases polynomially with respect to the number of contact patches or contact areas, and exponentially with respect to the horizon depth parameter.

Note, however, that fewer total calls may be made if one or more nodes are rejected (*i.e.*, they are invalid or duplicates) and hence their children are not generated. The number of calls may be further reduced by only attempting placements on contact areas within the robot’s reach.

Another important observation is that, as RHCP generates only one child node per contact patch-area pair (for a given parent node), it is not possible for the algorithm to guarantee completeness. That is to say, there may be possible motion plans that the planner fails to find due to it not considering other locations at which contacts could be formed between the same contact patch-area pair.

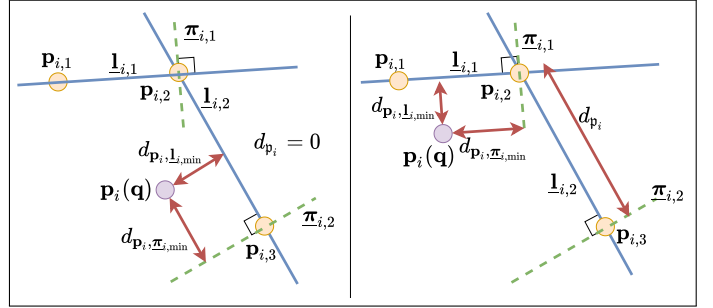


Figure 3: Illustration of primitives used in contact patch-specific potential field terms. Two scenarios are given for different positions of the contact patch (shown as a purple circle). The remaining path distance $d_{\mathbf{p}_i}$ is shown in red in the scenario on the right but is absent from the left scenario, since $d_{\mathbf{p}_i} = 0$ in this case.

Finally, compared to other CBM motion planners, RHCP is especially well suited to rapid re-planning in response to new information or changes in the environment. This is because the motion plan may be updated by merely repeating the previous planning cycle to generate a new next-step recommendation, rather than repeating a costly global planning operation. This is particularly useful if the environment is not fully mapped beforehand, as the robot can quickly update the plan as its sensors gather more data.

4. Potential-field-based Guide Path

Recall that the configuration-space guide path $\mathbf{q} \in \mathcal{Q}$ comprises a sequence of waypoint configurations

$$\mathbf{q} \triangleq (\mathbf{q}_1, \dots, \mathbf{q}_G).$$

We also define workspace waypoints for each contact patch \mathcal{P}_i , written as $\mathbf{p}_i \triangleq \{\mathbf{p}_i(\mathbf{q}) \in \mathbb{H}_p : \mathbf{q} \in \mathbf{q}\}$, where $\mathbf{p}_i(\mathbf{q}) : \mathcal{Q} \rightarrow \mathbb{H}_p$ denotes the workspace position of the coordinate frame attached to \mathcal{P}_i in configuration \mathbf{q} .

Each successive pair of waypoints $(\mathbf{p}_{i,j}, \mathbf{p}_{i,j+1})$ is used to define a dual quaternion line $\mathbf{l}_{i,j} \in \mathcal{H}_p \cap \underline{\mathcal{S}}$ (illustrated in Figure 3), written as [15]

$$\mathbf{l}_{i,j} \triangleq \mathbf{l}_{i,j} + \varepsilon (\mathbf{p}_{i,j} \times \mathbf{l}_{i,j}), \quad (7)$$

where $\mathbf{l}_{i,j} \in \mathbb{H}_p \cap \mathbb{S}^3$ is given by

$$\mathbf{l}_{i,j} \triangleq \frac{\mathbf{p}_{i,j+1} - \mathbf{p}_{i,j}}{\|\mathbf{p}_{i,j+1} - \mathbf{p}_{i,j}\|}. \quad (8)$$

We also define a dual quaternion plane $\underline{\mathcal{P}}_{i,j} \in \mathcal{H}$ attached to $\mathbf{p}_{i,j+1}$ whose normal vector is equal to $-\mathbf{l}_{i,j}$, written as [15]

$$\underline{\mathcal{P}}_{i,j} \triangleq -\mathbf{l}_{i,j} + \varepsilon \langle \mathbf{p}_{i,j+1}, -\mathbf{l}_{i,j} \rangle. \quad (9)$$

The closest line segment to $\mathbf{p}_i(\mathbf{q})$ is denoted $\mathbf{l}_{i,\min}$.² If multiple line segments are equally close to $\mathbf{p}_i(\mathbf{q})$, then

²Each line segment is treated as finite and bounded by the waypoints at each end for the purposes of this check.

that which results in the lowest overall potential is chosen. The waypoint terminating $\mathbf{l}_{i,\min}$ is denoted $\mathbf{p}_{i,\min}$, while the plane intersecting that point is denoted $\underline{\pi}_{i,\min}$. We thus define the contact patch-specific sub-field for contact patch \mathcal{P}_i as

$$U_{\mathcal{P}_i}(\mathbf{q}) \triangleq D_{\mathbf{p}_i, \mathbf{l}_{i,\min}} + \alpha \left(D_{\mathbf{p}_i, \underline{\pi}_{i,\min}} + D_{\mathbf{p}_i} \right), \quad (10)$$

where $\alpha \in (0, \infty)$ is a user-defined weighting term, and the terms $D_{\mathbf{p}_i, \mathbf{l}_{i,\min}} \in [0, \infty)$ and $D_{\mathbf{p}_i, \underline{\pi}_{i,\min}} \in [0, \infty)$ denote the point-to-line square distance between $\mathbf{p}_i(\mathbf{q})$ and $\mathbf{l}_{i,\min}$, and the point-to-plane square distance between $\mathbf{p}_i(\mathbf{q})$ and $\underline{\pi}_{i,\min}$, respectively [16].³ The term $D_{\mathbf{p}_i} \in [0, \infty)$ denotes the square of the distance *along the path* from $\mathbf{p}_{i,\min}$ to the final waypoint, given by

$$D_{\mathbf{p}_i} \triangleq \sum_{j=k+1}^{n_W-1} D_{\mathbf{p}_{i,j}, \mathbf{p}_{i,j+1}}, \quad (11)$$

where n_W is the number of waypoints, $\mathbf{l}_{i,k} = \mathbf{l}_{i,\min}$, and $D_{\mathbf{p}_{i,j}, \mathbf{p}_{i,j+1}}$ denotes the point-to-point square distance from $\mathbf{p}_{i,j}$ to $\mathbf{p}_{i,j+1}$ [16].

Each sub-field $U_{\mathcal{P}_i}(\mathbf{q})$ is minimised by keeping \mathcal{P}_i close to its guide path (minimising $D_{\mathbf{p}_i, \mathbf{l}_{i,\min}}$) and moving along the path towards the goal (minimising $D_{\mathbf{p}_i, \underline{\pi}_{i,\min}} + D_{\mathbf{p}_i}$).

For a given line segment, $U_{\mathcal{P}_i}(\mathbf{q})$ is non-negative and continuously differentiable with respect to \mathbf{q} . An illustration of $U_{\mathcal{P}_i}(\mathbf{q})$ for a guide path containing four waypoints over a 2D cross-section of the workspace is shown in Figure 4, whereas which line segment is serving as $\mathbf{l}_{i,\min}$ is highlighted by the regions shown in Figure 5. Both figures show how the potential field monotonically decreases as the contact patch \mathcal{P}_i moves from the initial waypoint $\mathbf{p}_i(\mathbf{q}_1)$ to the final waypoint $\mathbf{p}_i(\mathbf{q}_4)$.

Having defined the sub-field for each patch \mathcal{P}_i , the full potential field is written

$$U(\mathbf{q}) \triangleq \sum_{i=1}^{n_{\mathcal{R}}} U_{\mathcal{P}_i}(\mathbf{q}). \quad (12)$$

5. Posture Generation

To guarantee that a given stance is feasible, multi-contact planners must find safe whole-body transition configurations that allow the robot to realise the intended stance while respecting certain constraints (*e.g.*, avoiding collisions, maintaining balance, *etc.*). The task of finding such a configuration for a given stance is known as the '*posture generation problem*'. Expanding upon our previous work [14], we propose a novel posture generation method that improves upon the state-of-the-art by:

³Note that in Figure 3 the signed distances $d_{\mathbf{p}_i, \mathbf{l}_{i,\min}}$, $d_{\mathbf{p}_i, \underline{\pi}_{i,\min}}$ and $d_{\mathbf{p}_i}$ are shown, whereas (10) uses the square distances, given by $D_{\mathbf{p}_i, \mathbf{l}_{i,\min}} = d_{\mathbf{p}_i, \mathbf{l}_{i,\min}}^2$, $D_{\mathbf{p}_i, \underline{\pi}_{i,\min}} = d_{\mathbf{p}_i, \underline{\pi}_{i,\min}}^2$ and $D_{\mathbf{p}_i} = d_{\mathbf{p}_i}^2$. This is because the square distances are differentiable everywhere, whereas the signed distance time derivatives are not defined at zero [16].

- Guaranteeing, for every node returned, that a feasible linking trajectory exists for the robot to safely transition into that node's stance.
- Generating the stance, transition configuration and linking trajectory *simultaneously*, removing the need for secondary planning stages and hence reducing the overall complexity of the planning pipeline.
- Returning nodes faster than traditional methods by re-formulating the problem as a series of linearly constrained quadratic programs, rather than as a single non-linear optimisation problem.

The posture generator is based on a VFI constrained controller in the same form as (2), which drives a model of the robot into an appropriate stance. This allows us to simultaneously plan new stances while implicitly generating the transition configuration and whole-body trajectory, which can be tracked by the real robot. A flowchart summarising the approach is given in Figure 6.

Each posture generator call comprises the following three stages (depicted in Figure 7):

- Given the parent configuration \mathbf{q}_P and stance s_P , the breaking stage finds a configuration that allows the robot to safely break contact c^* , returning the stance $s_B = s_P \setminus \{c^*\}$, configuration $\mathbf{q}_B \in \mathcal{F}_{s_P} \cap \mathcal{F}_{s_B}$, and trajectory $\mathcal{T}_{P,B}$ linking \mathbf{q}_P to \mathbf{q}_B .
- The transition stage moves the desired contact patch \mathcal{P}^* to the intended contact area \mathcal{A}^* , returning the configuration $\mathbf{q}_T \in \mathcal{F}_{s_B}$ and trajectory $\mathcal{T}_{B,T}$.
- The placement optimisation stage optimises the location of \mathcal{P}^* on \mathcal{A}^* , forming a new contact c_{new} , and returning the stance $s_O = s_B \cup \{c_{\text{new}}\}$, configuration $\mathbf{q}_O \in \mathcal{F}_{s_B} \cap \mathcal{F}_{s_O}$ and trajectory $\mathcal{T}_{T,O}$.
- The final result is a child node $\mathbf{n}_c = (\mathbf{n}_P, s_O, \mathbf{q}_O, \mathcal{T}_{P,O})$, where $\mathcal{T}_{P,O}$ is the concatenation of $\mathcal{T}_{P,B}$, $\mathcal{T}_{B,T}$ and $\mathcal{T}_{T,O}$.

Each time a quadratic program is solved to find the instantaneous control input, numerical integration is used to update the robot configuration for the next time step in the corresponding configuration-space trajectory. The functions of \mathbf{q} (*e.g.*, the Jacobian matrices) are then recalculated, and the cycle repeats. This continues until either the stage's stopping criteria are satisfied or an evaluation limit is reached.

5.1. VFIs under discretisation effects

When operating in continuous time, VFI constraints ensure that any robot entities outside of a restricted zone at time $t = 0$ will continue to be so for all times $t > 0$. However, in RHCP we use discrete numerical integration steps to obtain the next configuration every time an instantaneous control input is returned by the posture generator. In order to minimise the number of control cycles,

5.1 VFIs under discretisation effects

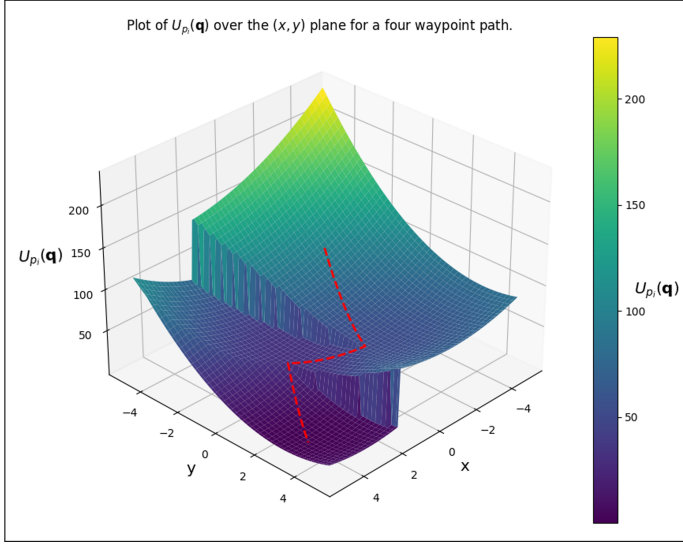


Figure 4: 3D plot of the potential field term $U_{P_i}(\mathbf{q})$ over the (x, y) plane for an example guide path (shown in red).

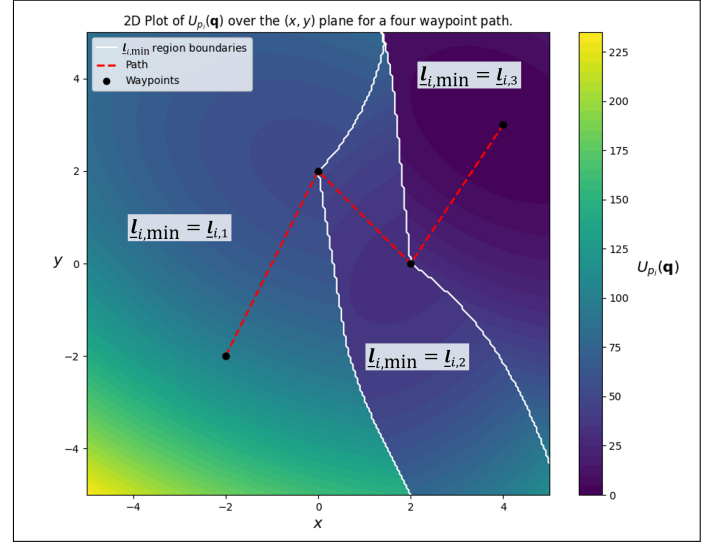


Figure 5: 2D cross-section plot of $U_{P_i}(\mathbf{q})$ over the (x, y) plane for the example path in Figure 4. The white boundaries indicate which line segment serves as $\underline{L}_{i,\min}$.

and hence also reduce the amount of time required to plan, it is desirable to use the largest integration step size possible. Therefore the assumption of continuous time is violated and, since each integration step acts as a zero-order hold, the robot may briefly enter the restricted zone, risking unsafe behaviour or an unfeasible optimisation problem. To address this, we artificially inflate the boundaries of each restricted zone by a buffer $b_d \in (0, \infty)$, which can be given as a function of the robot's maximum speed and the integration period.

When keeping a robot body outside of a restricted zone, the boundary of that zone is expanded by the buffer (shown on the *left* in Figure 8). We thus re-write the constraint (4) for keeping outside a restricted zone as

$$-\mathbf{J}_d \dot{\mathbf{q}} \leq \eta_d (\tilde{d}(\mathbf{q}) - b_d). \quad (13)$$

Likewise, when staying inside a safe zone, the constraint is *tightened* by the buffer (shown on the *right* in Figure 8), and constraint (5) is rewritten

$$\mathbf{J}_d \dot{\mathbf{q}} \leq -\eta_d (\tilde{d}(\mathbf{q}) + b_d). \quad (14)$$

Furthermore, to ensure that there is always at least one solution to problem (2), we improve upon constraints (13) and (14) in order to guarantee that they are always satisfied by $\dot{\mathbf{q}} = \mathbf{0}$. For example, when $\dot{\mathbf{q}} = \mathbf{0}$, (13) is reduced to $0 \leq \tilde{d}(\mathbf{q}) - b_d$. If the robot violates the inflated boundaries but does not violate the original boundaries (*i.e.*, $0 \leq \tilde{d}(\mathbf{q}) < b_d$), we have $\tilde{d}(\mathbf{q}) - b_d < 0$, and hence $\dot{\mathbf{q}} = \mathbf{0}$ no longer satisfies (13) (shown in Figure 9).

To overcome this problem, we add a slack variable $s_d \in [0, \max(0, -\eta_d(\tilde{d}(\mathbf{q}) - b_d))]$ to the constraint, resulting in

$$-\mathbf{J}_d \dot{\mathbf{q}} \leq \eta_d (\tilde{d}(\mathbf{q}) - b_d) + s_d. \quad (15)$$

Therefore, if $0 \leq \tilde{d}(\mathbf{q}) < b_d$ and the robot takes the maximum allowable slack $s_d = -\eta_d(\tilde{d}(\mathbf{q}) - b_d)$, then (15) becomes $-\mathbf{J}_d \dot{\mathbf{q}} \leq 0$ to which $\dot{\mathbf{q}} = \mathbf{0}$ is a valid solution. Note that $-\mathbf{J}_d \dot{\mathbf{q}} \leq 0 \iff \mathbf{J}_d \dot{\mathbf{q}} \geq 0 \iff \dot{d} \geq 0$; therefore, the robot cannot make any further progress towards the boundary of the restricted zone. Additionally, if the robot is inside the buffered safe zone (and hence $\tilde{d}(\mathbf{q}) - b_d \geq 0$), then $-\eta_d(\tilde{d}(\mathbf{q}) - b_d) \leq 0$, meaning that the maximum allowable slack is zero. Hence, only the minimum slack required for $\dot{\mathbf{q}} = \mathbf{0}$ to be a valid solution is ever permitted.

Analogously, when inside a safe zone, if the robot body lies inside the original safe zone but outside of the buffered safe zone (as shown in Figure 9), we have $-b_d < \tilde{d}(\mathbf{q}) \leq 0$, which implies that $\tilde{d}(\mathbf{q}) + b_d > 0$ and hence $\dot{\mathbf{q}} = \mathbf{0}$ does not satisfy (14). In this case, the slack variable is written as $s_d \in [0, \max(0, \eta_d(\tilde{d}(\mathbf{q}) + b_d))]$ so that (14) is rewritten as

$$\mathbf{J}_d \dot{\mathbf{q}} \leq -\eta_d (\tilde{d}(\mathbf{q}) + b_d) + s_d, \quad (16)$$

making $\dot{\mathbf{q}} = \mathbf{0}$ a feasible solution.

Finally, problem (2) is rewritten as

$$\begin{aligned} \mathbf{u} \in \operatorname{argmin}_{\dot{\mathbf{q}}, \mathbf{s}} \quad & \Psi(\mathbf{q}, \dot{\mathbf{q}}) + \lambda^2 \|\dot{\mathbf{q}}\|_2^2 + \beta^2 \|\mathbf{s}\|_2^2 \\ \text{subject to} \quad & \mathbf{W}_1 \dot{\mathbf{q}} \preceq \mathbf{w}_1 + \mathbf{s} \\ & \mathbf{W}_2 \dot{\mathbf{q}} = \mathbf{w}_2 \\ & \mathbf{v}_{\min} \preceq \dot{\mathbf{q}} \preceq \mathbf{v}_{\max} \\ & \mathbf{0}_\ell \preceq \mathbf{s} \preceq \mathbf{s}_{\max}, \end{aligned} \quad (17)$$

where $\beta, \lambda \in (0, \infty)$ and $\mathbf{s} = [s_1 \ \cdots \ s_\ell]^T$ is the vector of slack variables. The vector pairs $\mathbf{v}_{\min}, \mathbf{v}_{\max}$ and $\mathbf{0}_\ell, \mathbf{s}_{\max}$ impose lower and upper limits on $\dot{\mathbf{q}}$ and \mathbf{s} , respectively. The task function $\Psi(\mathbf{q}, \dot{\mathbf{q}})$ defines the task for a given stage

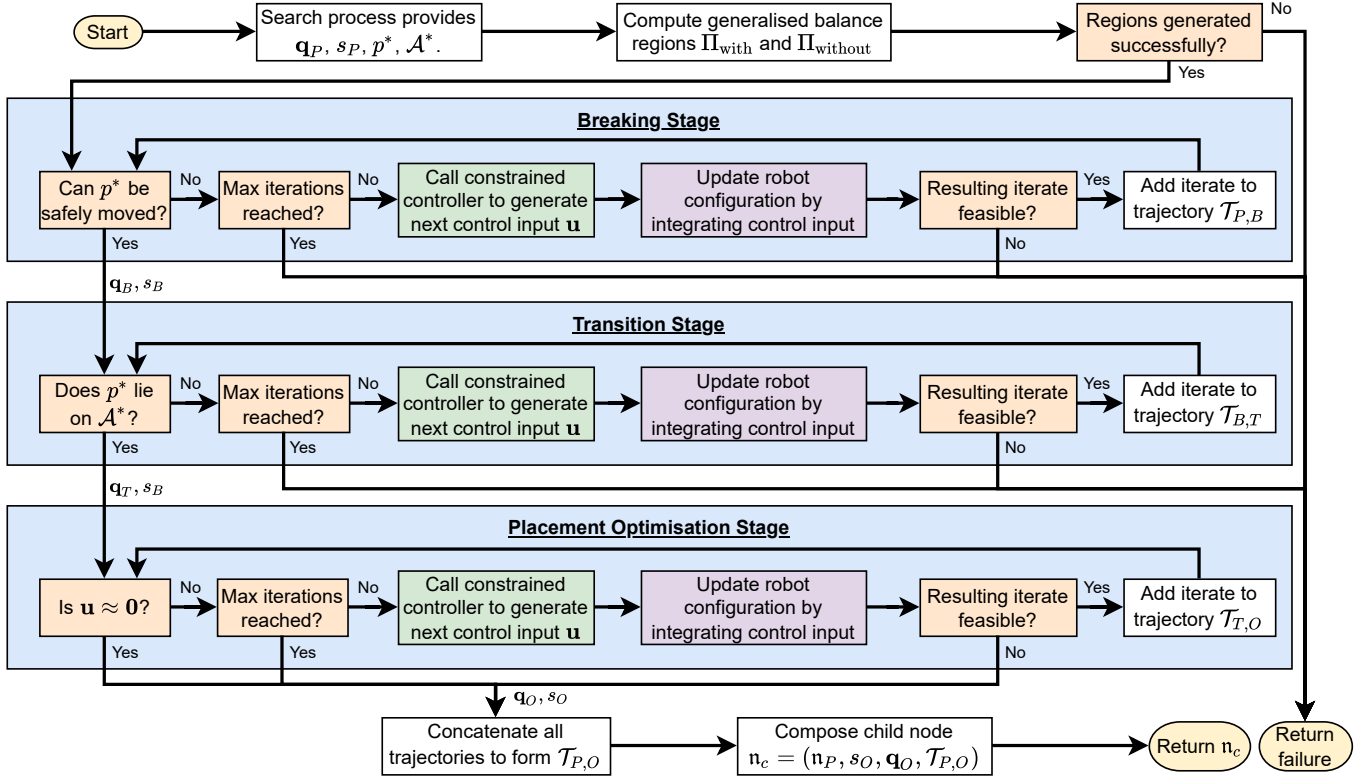


Figure 6: Flowchart summarising our proposed posture generator.

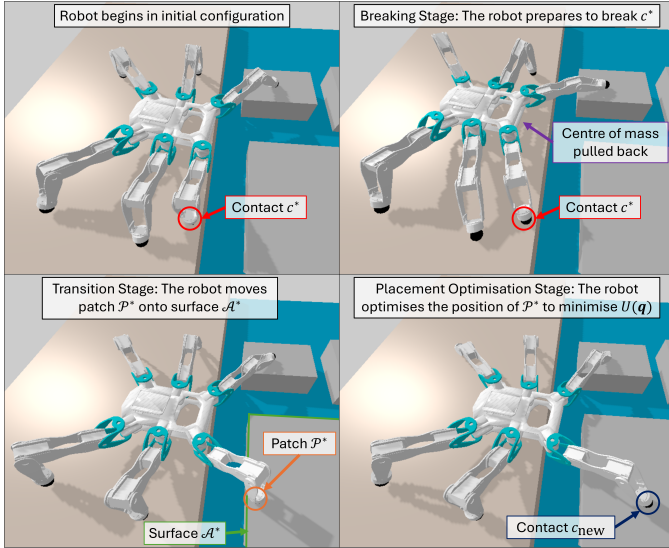


Figure 7: Illustration of each posture generation stage.

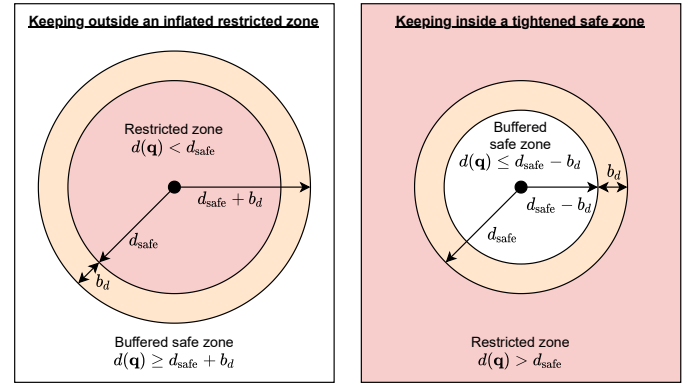


Figure 8: Buffer zones applied to VFI constraints when keeping outside an inflated restricted zone (left) (13) and inside a tightened safe zone (right) (14)

5.2. Constraints and Objectives For the Posture Generator

In this section the VFI constraints and objective functions $\Psi(\dot{q})$ for each stage of the posture generator are derived.

5.2.1. Common Constraints to All Stages

Five types of constraints apply to all stages of the posture generator: avoiding collisions and self-collisions; maintaining balance; preventing contacts from sliding; avoiding excessive torso tilting; and respecting the limits and topologies of the optimisation variables.

(breaking, transition, placement optimisation) in the form

$$\Psi(\dot{q}) = \sum_{i=1}^{n_{\bar{x}}} \|\mathbf{J}_{\bar{x}_i} \dot{q} + \eta_o \tilde{x}_i\|_2^2. \quad (18)$$

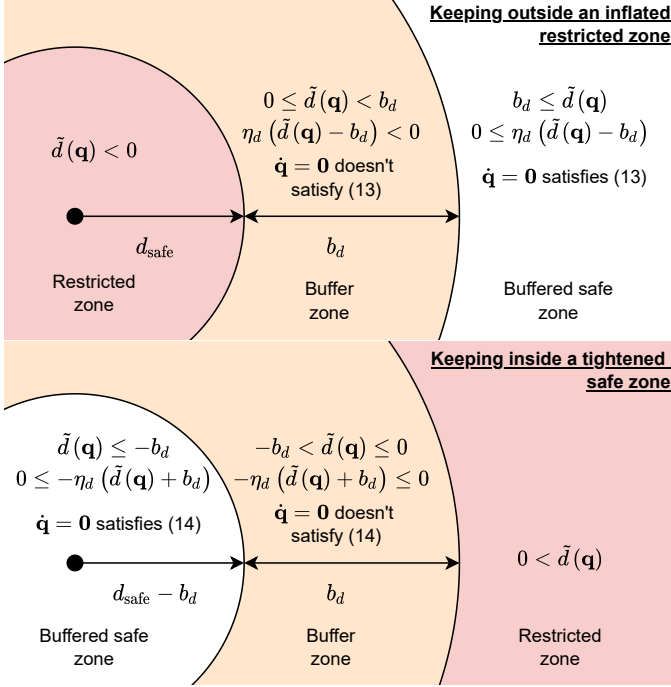


Figure 9: Slack variables for keeping outside an inflated restricted zone (top) or inside a tightened safe zone (bottom).

Collision and self-collision avoidance constraints. We define $\mathcal{H}_B \subset \mathcal{H}$ as the set of dual quaternion primitives representing each robot body part $\underline{\mathbf{h}}_i \in \mathcal{H}_B$ for the purposes of collisions, which may be planes, cylinders or spheres [16]. The environment is modelled as a set of convex obstacles, whose surfaces are described by the set $\Pi_{\mathcal{O}} \triangleq \{\underline{\pi}_1, \dots, \underline{\pi}_{n_{\mathcal{O}}}\}$, wherein each element $\underline{\pi}_j \in \mathcal{H}$ is an infinite plane whose normal vector is directed outside of the obstacle. The subset of planes that are forbidden from colliding with the robot body part $\underline{\mathbf{h}}_i$ is written as $\Pi_{\mathcal{OB}_i}(\underline{\mathbf{h}}_i) \subseteq \Pi_{\mathcal{O}}$. The planes in $\Pi_{\mathcal{OB}_i}$ are selected based on the position of the robot primitive $\underline{\mathbf{h}}_i$ in the workspace, similar to the approach used to model small obstacles in [17]. An illustration of this process is shown in Figure 10. For instance, when a robot body part is in the free region 3, planes $\underline{\pi}_3$ and $\underline{\pi}_5$ prevent the robot part from colliding with block \mathcal{O}_2 and wall \mathcal{O}_3 and allow the robot body part to be moved to free region 2 or free region 4. If the robot part moves to free region 2, then only planes $\underline{\pi}_1$ and $\underline{\pi}_5$ are activated, allowing the robot part to move to either free region 1 or free region 3. Although this process is simplified in Figure 10, it is general and we use it to represent non-convex tridimensional free workspaces.

We thus write the signed distance between a given robot body primitive $\underline{\mathbf{h}}_i \in \mathcal{H}_B$ and a given plane $\underline{\pi}_j \in \Pi_{\mathcal{OB}_i}$ as $d_{\underline{\mathbf{h}}_i, \underline{\pi}_j} \in \mathbb{R}$. The Jacobian matrix of $d_{\underline{\mathbf{h}}_i, \underline{\pi}_j}$ is written as $\mathbf{J}_{\underline{\mathbf{h}}_i, \underline{\pi}_j} \triangleq \mathbf{J}_{\underline{\mathbf{h}}_i, \underline{\pi}_j}(\mathbf{q})$ [16]. Hence, the unbuffered distance term is written as $\tilde{d}_{\underline{\mathbf{h}}_i, \underline{\pi}_j} \triangleq d_{\underline{\mathbf{h}}_i, \underline{\pi}_j} - d_{\text{safe}, \mathcal{O}}$ and the collision avoidance requirement is stated as $\tilde{d}_{\underline{\mathbf{h}}_i, \underline{\pi}_j} \geq b_d$. The collision avoidance constraint is thus defined, in the same

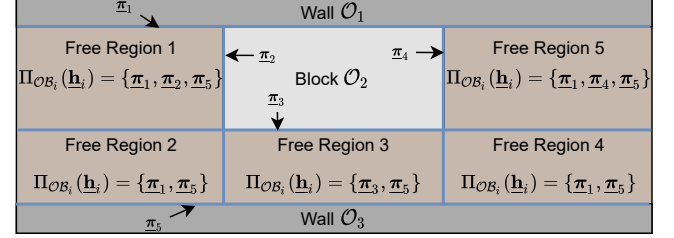


Figure 10: Illustration of how collision planes are assigned for a given robot body part based on its position in a non-convex free space. The collision plane with the ground is omitted for clarity.

form as (15),

$$-\mathbf{J}_{\underline{\mathbf{h}}_i, \underline{\pi}_j} \dot{\mathbf{q}} \leq \eta_d (\tilde{d}_{\underline{\mathbf{h}}_i, \underline{\pi}_j} - b_d) + s_{\underline{\mathbf{h}}_i, \underline{\pi}_j}, \quad \forall \underline{\pi}_j \in \Pi_{\mathcal{OB}_i}, \forall \underline{\mathbf{h}}_i \in \mathcal{H}_B. \quad (19)$$

These constraints can be represented in stacked matrix/vector form as

$$\begin{aligned} \mathbf{W}_{\mathcal{OB}} &= [-\mathbf{J}_1^\top \quad \dots \quad -\mathbf{J}_{n_{\mathcal{OB}}}^\top]^\top \\ \mathbf{w}_{\mathcal{OB}} &= [\eta_d (\tilde{d}_1 - b_d) \quad \dots \quad \eta_d (\tilde{d}_{n_{\mathcal{OB}}} - b_d)]^\top \\ \mathbf{s}_{\mathcal{OB}} &= [s_1 \quad \dots \quad s_{n_{\mathcal{OB}}}]^\top, \end{aligned} \quad (20)$$

where $n_{\mathcal{OB}}$ is the number of robot body parts in \mathcal{H}_B multiplied by the number of planes in each corresponding set $\Pi_{\mathcal{OB}_i}$. Thus, the complete collision avoidance constraint may be evaluated as

$$\mathbf{W}_{\mathcal{OB}} \dot{\mathbf{q}} \preceq \mathbf{w}_{\mathcal{OB}} + \mathbf{s}_{\mathcal{OB}}. \quad (21)$$

The process for self-collision avoidance is similar. We denote by $\mathcal{Y}_B(\underline{\mathbf{h}}) \subset \mathcal{H}_B$ the subset of primitives in \mathcal{H}_B that are forbidden from colliding with $\underline{\mathbf{h}} \in \mathcal{H}_B$. The self-collision constraint is thus written as

$$-\mathbf{J}_{\underline{\mathbf{h}}, \underline{\mathbf{y}}} \dot{\mathbf{q}} \leq \eta_d (\tilde{d}_{\underline{\mathbf{h}}, \underline{\mathbf{y}}} - b_d) + s_{\underline{\mathbf{h}}, \underline{\mathbf{y}}}, \quad \forall \underline{\mathbf{y}} \in \mathcal{Y}_B(\underline{\mathbf{h}}), \forall \underline{\mathbf{h}} \in \mathcal{H}_B. \quad (22)$$

These constraints may be expressed in stacked matrix/vector form in the same manner as (20), being written as

$$\mathbf{W}_{\mathcal{BB}} \dot{\mathbf{q}} \preceq \mathbf{w}_{\mathcal{BB}} + \mathbf{s}_{\mathcal{BB}}. \quad (23)$$

Balance constraint. In order to maintain quasi-static balance during the posture generation process, the robot must position its COM in such a way that feasible forces can be generated at the contacts that will counteract gravity, result in no net force or moment, and prevent contacts from slipping. Bretl and Lall [20] show that, for any set of point contacts, the region of COM positions satisfying these conditions is a vertical prism with a convex cross-section on the horizontal plane. They also present an efficient interior-point algorithm to compute a conservative approximation of this region (*the generalised support region*) to within a user-defined level of precision. We adopt

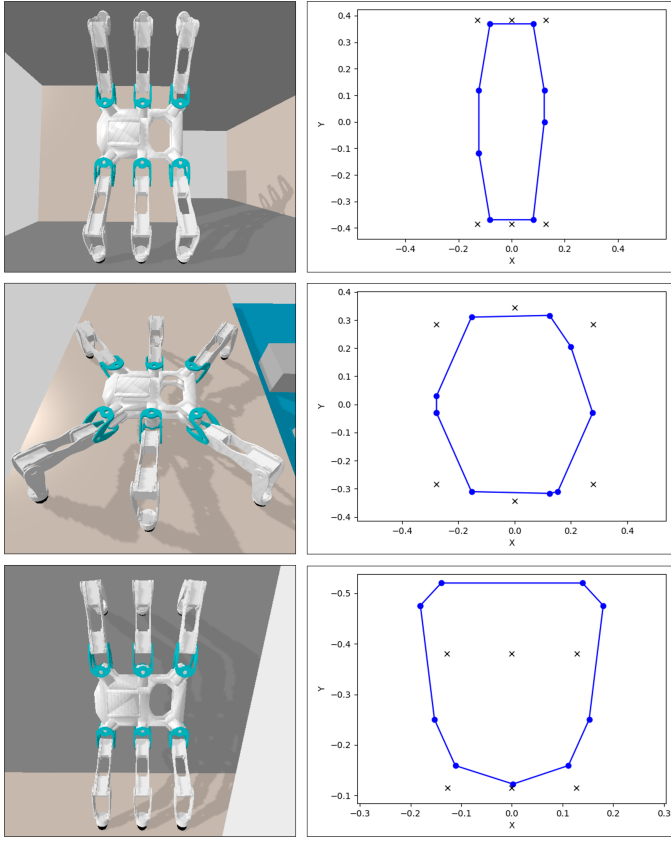


Figure 11: The Corin hexapod in different configurations (left) and their associated generalised support regions (right). In each figure, the positions of the contacts are shown as black crosses.

this method for our posture generation process with two small modifications.

Firstly, we apply limits on the magnitude of the forces that the robot is permitted to generate at each contact, constraining each 3D force vector \mathbf{f}_i such that $\mathbf{f}_{\min} \preceq \mathbf{f}_i \preceq \mathbf{f}_{\max}$. Secondly, we use polyhedral approximations of the Coulomb friction cones [21], reducing the algorithm in [20] to a series of linear optimisation problems with linear constraints, allowing it to be solved extremely quickly. Examples of generalised support regions for three different scenarios are shown in Figure 11.⁴

Having computed the generalised support region, we define $\Pi_{\text{balance}} \triangleq \{\pi_{B_1}, \dots, \pi_{B_m}\}$ as the set of vertical planes describing the boundaries of the region. The normal vector of each plane is directed outside of the region. Writing the point-to-plane signed distance between the centre of mass position $\mathbf{p}_C(\mathbf{q}) \in \mathcal{W}$ and the plane $\pi_{B_i} \in \Pi_{\text{balance}}$ as $d_{\mathbf{p}_C, \pi_{B_i}} \in \mathbb{R}$, and the Jacobian matrix

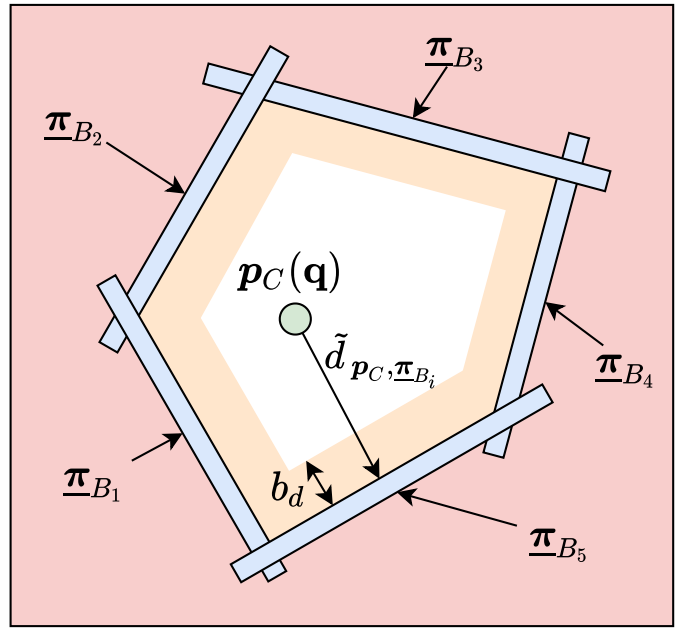


Figure 12: Illustration of the quasi-static balance VFI constraint (24) for a 2D cross section, with $\pi_{B_1}, \dots, \pi_{B_5} \in \Pi_{\text{balance}}$.

of $d_{\mathbf{p}_C, \pi_{B_i}}$ as $\mathbf{J}_{\mathbf{p}_C, \pi_{B_i}}$ [16], the unbuffered distance term is given as $\tilde{d}_{\mathbf{p}_C, \pi_{B_i}} \triangleq d_{\mathbf{p}_C, \pi_{B_i}} - d_{\text{safe}, B}$ and the requirement is stated as $\tilde{d}_{\mathbf{p}_C, \pi_{B_i}} \leq -b_d$, illustrated in Figure 12.

The static balance constraint is thus defined, in the same form as (16),

$$\mathbf{J}_{\mathbf{p}_C, \pi_{B_i}} \dot{\mathbf{q}} \leq -\eta_d (\tilde{d}_{\mathbf{p}_C, \pi_{B_i}} + b_d) + s_{\mathbf{p}_C, \pi_{B_i}}, \forall \pi_{B_i} \in \Pi_{\text{balance}}. \quad (24)$$

As before, these constraints are expressed in stacked matrix/vector form as

$$\mathbf{W}_{\text{Bal}} \dot{\mathbf{q}} \leq \mathbf{w}_{\text{Bal}} + \mathbf{s}_{\text{Bal}}. \quad (25)$$

Preventing foot sliding. When the posture generator is called, it first determines which contact patches are free to move during a particular stage. For instance, during the breaking stage no contact patches are free to move, while in the transition and placement optimisation stages only \mathcal{P}^* is free to move. Those contact patches that are *not* free to move make up the set $\mathcal{R}_{\text{fixed}} \subset \mathcal{R}$, and the posture generator must ensure that their positions do not change.

Therefore, we constrain the centroid of each fixed contact patch, written as \mathbf{p}_i for $\mathcal{P}_i \in \mathcal{R}_{\text{fixed}}$, to remain inside a small sphere of radius R_{slip} centred on its desired location \mathbf{p}_{d_i} . Writing the point-to-point square distance between \mathbf{p}_i and \mathbf{p}_{d_i} as $D_{\mathbf{p}_i, \mathbf{p}_{d_i}}$, we define the unbuffered distance term as $\tilde{D}_{\mathbf{p}_i, \mathbf{p}_{d_i}} \triangleq D_{\mathbf{p}_i, \mathbf{p}_{d_i}} - R_{\text{slip}}^2$ and state the requirement as $\tilde{D}_{\mathbf{p}_i, \mathbf{p}_{d_i}} \leq -b_d^2$ (illustrated in Figure 13). The constraint

⁴The support regions shown in Figure 11 do not meet the contact locations, even in the middle case where they all lie on a horizontal surface, because the forces realised at each contact are limited. When the COM is very close to a single contact, the forces required at that contact to support the robot's balance become large enough to exceed this upper limit, and hence the support regions are cut-off before reaching the contact points.

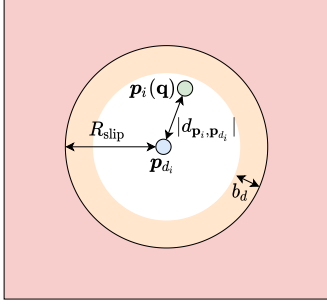


Figure 13: Illustration of the contact slippage VFI constraint (26) for a 2D cross section. Note that $d_{\mathbf{p}_i, \mathbf{p}_{d_i}} = d_{\mathbf{p}_i, \mathbf{p}_{d_i}}^2$.

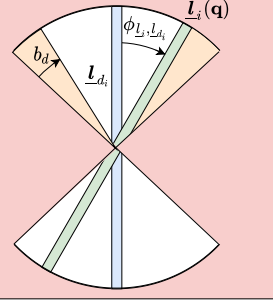


Figure 14: Illustration of the angular VFI constraint (28) for a 2D cross section.

is thus given as

$$\mathbf{J}_{\mathbf{p}_i, \mathbf{p}_{d_i}} \dot{\mathbf{q}} \leq -\eta_d \left(\tilde{d}_{\mathbf{p}_i, \mathbf{p}_{d_i}} + b_d^2 \right) + s_{\mathbf{p}_i, \mathbf{p}_{d_i}}, \forall \mathcal{P}_i \in \mathcal{R}_{\text{fixed}}, \quad (26)$$

and is expressed in stacked matrix/vector form as before

$$\mathbf{W}_{\mathcal{R}} \dot{\mathbf{q}} \preceq \mathbf{w}_{\mathcal{R}} + \mathbf{s}_{\mathcal{R}}. \quad (27)$$

Preventing excessive tilting: In order to prevent the robot from assuming extreme root (*i.e.*, the robot base/torso) orientations that are not conducive to continued progress, we constrain the root orientation to lie within a maximum tolerance from a desired value.

The desired root orientation is defined as that of the closest point on the whole-body guide path \mathbf{q} to the current configuration. We then obtain Plücker lines in dual quaternion form [15] describing the x , y and z axes of the robot's torso frame with respect to the world frame ($\mathbf{l}_x, \mathbf{l}_y, \mathbf{l}_z \in \mathcal{H}_p \cap \mathcal{S}$, respectively) as well as those for the desired torso orientation (denoted $\mathbf{l}_{d_x}, \mathbf{l}_{d_y}, \mathbf{l}_{d_z} \in \mathcal{H}_p \cap \mathcal{S}$). Using the angular distance function between two lines $d_{\phi_{\mathbf{l}_1}, \phi_{\mathbf{l}_2}}$ and its Jacobian matrix $\mathbf{J}_{\phi_{\mathbf{l}_1}, \phi_{\mathbf{l}_2}}$ as described in [18], we define the error term as $\tilde{d}_{\phi_{\mathbf{l}_1}, \phi_{\mathbf{l}_2}} \triangleq d_{\phi_{\mathbf{l}_1}, \phi_{\mathbf{l}_2}} - d_{\text{safe}, \phi}$ and state the requirement as $\tilde{d}_{\phi_{\mathbf{l}_1}, \phi_{\mathbf{l}_2}} \leq -b_d$ (illustrated in Figure 14). The constraint is thus given as

$$\mathbf{J}_{\phi_{\mathbf{l}_i}, \phi_{\mathbf{l}_{d_i}}} \dot{\mathbf{q}} \leq -\eta_d \left(\tilde{d}_{\phi_{\mathbf{l}_i}, \phi_{\mathbf{l}_{d_i}}} + b_d \right) + s_{\phi_{\mathbf{l}_i}, \phi_{\mathbf{l}_{d_i}}}, \forall \mathbf{l}_i \in \{\mathbf{l}_x, \mathbf{l}_y, \mathbf{l}_z\}. \quad (28)$$

As before, this is written in matrix/vector form as

$$\mathbf{W}_\phi \dot{\mathbf{q}} \preceq \mathbf{w}_\phi + \mathbf{s}_\phi. \quad (29)$$

Respecting variable limits and topologies: As discussed in Section 2, this work assumes that configuration vectors take the form $\mathbf{q} = [\text{vec}_4(\mathbf{r})^\top \text{vec}_3(\mathbf{p})^\top \boldsymbol{\theta}^\top]^\top$, where the term $\mathbf{r} \in \mathbb{S}^3$ represents the orientation of the robot root. Due to the presence of this term, the optimisation must be constrained to ensure that $\dot{\mathbf{q}}$ respects the properties of the underlying topology of unit quaternions—*i.e.*,

the condition $\|\mathbf{r}\| = \text{vec}_4(\mathbf{r})^T \text{vec}_4(\mathbf{r}) = 1$ must be maintained. By taking the time derivative of this expression, we obtain the constraint

$$\text{vec}_4(\mathbf{r})^T \text{vec}_4(\dot{\mathbf{r}}) = 0, \quad (30)$$

which can be expressed in terms of $\dot{\mathbf{q}}$ by defining

$$\mathbf{R} = \begin{bmatrix} \text{vec}_4(\mathbf{r})^T & \mathbf{0}_{3+n_\theta}^\top \end{bmatrix},$$

and hence writing $\mathbf{R}\dot{\mathbf{q}} = 0$.

Additionally, given limits on \mathbf{q} in the form $\mathbf{q}_{\min}, \mathbf{q}_{\max} \in \mathbb{R}^n$, we constrain $\dot{\mathbf{q}}$ such that $\mathbf{q}_{\min} \preceq \mathbf{q} \preceq \mathbf{q}_{\max}$ (similar to [18]) by writing the constraint

$$\eta_d (\mathbf{q}_{\min} - \mathbf{q} + b_d) \preceq \dot{\mathbf{q}} \preceq \eta_d (\mathbf{q}_{\max} - \mathbf{q} - b_d). \quad (31)$$

We define

$$\begin{aligned} \mathbf{w}_{\min} &= \eta_d (\mathbf{q}_{\min} - \mathbf{q} + b_d), \\ \mathbf{w}_{\max} &= \eta_d (\mathbf{q}_{\max} - \mathbf{q} - b_d), \end{aligned}$$

and thus (31) is rewritten as $\mathbf{w}_{\min} \preceq \dot{\mathbf{q}} \preceq \mathbf{w}_{\max}$.

5.2.2. Breaking Stage

The breaking stage brings the robot's centre of mass into a position such that contact c^* is not required for the robot's balance and can thus be safely broken. To begin, the posture generator computes two generalised support regions [20], one *with* and one *without* contact c^* , whose respective sets of planes are denoted Π_{with} and Π_{without} . We can thus formalise the breaking stage's requirement as

$$d_{\mathbf{p}_C, \pi_{B_i}} \leq -b_d, \forall \pi_{B_i} \in \Pi_{\text{without}}, \quad (32)$$

where $d_{\mathbf{p}_C, \pi_{B_i}}$ denotes the point-to-plane signed distance between the robot's centre of mass \mathbf{p}_C and each plane $\pi_{B_i} \in \Pi_{\text{without}}$ [16].

If condition (32) is satisfied by the starting configuration, then the breaking stage is skipped, with the robot proceeding to the transition stage. If the breaking stage is not skipped, then we define $\mathbf{l}_{\text{cent}} \in \mathcal{H}_p \cap \mathcal{S}$ as the line parallel to the gravity vector that intersects the centroid of the region Π_{without} . Writing the point-to-line square distance between \mathbf{p}_C and \mathbf{l}_{cent} as $D_{\mathbf{p}_C, \mathbf{l}_{\text{cent}}} \in [0, \infty)$, we define the task function as

$$\Psi_B(\dot{\mathbf{q}}) = \|\mathbf{J}_{\mathbf{p}_C, \mathbf{l}_{\text{cent}}} \dot{\mathbf{q}} + \eta_o D_{\mathbf{p}_C, \mathbf{l}_{\text{cent}}}\|_2^2, \quad (33)$$

where $\mathbf{J}_{\mathbf{p}_C, \mathbf{l}_{\text{cent}}}$ denotes the Jacobian matrix of $D_{\mathbf{p}_C, \mathbf{l}_{\text{cent}}}$. Minimising $\Psi_B(\dot{\mathbf{q}})$ drives the robot's COM from Π_{with} into Π_{without} (illustrated in Figure 15).

The constraints imposed during the breaking stage include avoiding collisions (19) and self-collisions (22), maintaining quasi-static balance (by keeping \mathbf{p}_C inside the safe zone described by Π_{with}) (24), maintaining all existing contacts (*i.e.*, $\mathcal{R}_{\text{fixed}} = \mathcal{R}$) (26), avoiding excessive root rotations (28), and respecting the variable bounds and topologies (30), (31). The optimisation problem is hence written

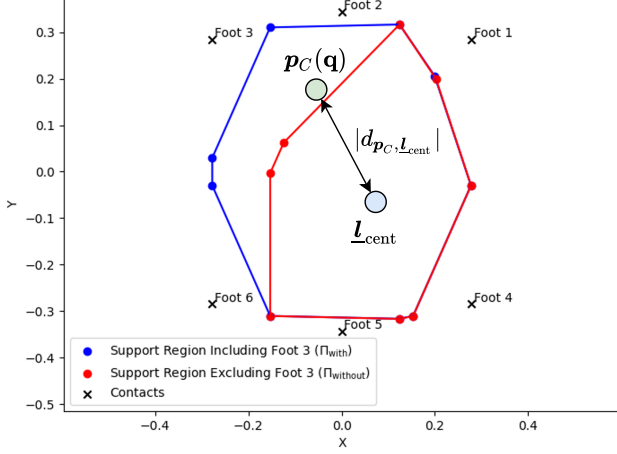


Figure 15: Illustration of the breaking stage task function (33). The goal is to move p_C toward l_{cent} so that the contact, in this case foot 3, can be safely broken.

as

$$\begin{aligned} \mathbf{u} \in \operatorname{argmin}_{\dot{\mathbf{q}}, \mathbf{s}} \quad & \Psi_B + \lambda^2 \|\dot{\mathbf{q}}\|_2^2 + \beta^2 \|\mathbf{s}\|_2^2 \\ \text{subject to} \quad & \mathbf{W}_B \dot{\mathbf{q}} \preceq \mathbf{w}_B + \mathbf{s}_B \\ & \mathbf{R} \dot{\mathbf{q}} = 0 \\ & \mathbf{w}_{\min} \preceq \dot{\mathbf{q}} \preceq \mathbf{w}_{\max} \\ & \mathbf{v}_{\min} \preceq \mathbf{s} \preceq \mathbf{v}_{\max} \\ & \mathbf{0}_{\ell} \preceq \mathbf{s} \preceq \mathbf{s}_{\max}, \end{aligned} \quad (34)$$

where

$$\mathbf{W}_B = \begin{bmatrix} \mathbf{W}_{OB} \\ \mathbf{W}_{BB} \\ \mathbf{W}_{\text{Bal}} \\ \mathbf{W}_{\mathcal{R}} \\ \mathbf{W}_{\phi} \end{bmatrix}, \quad \mathbf{w}_B = \begin{bmatrix} \mathbf{w}_{OB} \\ \mathbf{w}_{BB} \\ \mathbf{w}_{\text{Bal}} \\ \mathbf{w}_{\mathcal{R}} \\ \mathbf{w}_{\phi} \end{bmatrix}, \quad \mathbf{s}_B = \begin{bmatrix} \mathbf{s}_{OB} \\ \mathbf{s}_{BB} \\ \mathbf{s}_{\text{Bal}} \\ \mathbf{s}_{\mathcal{R}} \\ \mathbf{s}_{\phi} \end{bmatrix}. \quad (35)$$

The control input \mathbf{u} is numerically integrated to update the robot configuration. If the resulting configuration satisfies condition (32), then the breaking stage terminates and the process proceeds to the transition stage.

If condition (32) is *not* satisfied, then the process repeats, generating a new control input. If a user-defined maximum number of integration steps is reached without satisfying condition (32), then the posture generator returns a failure state.

5.2.3. Transition Stage

The transition stage brings patch \mathcal{P}^* into contact with the area \mathcal{A}^* , modelled as a plane $\underline{\pi}_{\mathcal{A}^*} \in \mathcal{S}$ with normal pointing outwards from the perspective of the object on which it is attached, with boundaries described by the set of planes Π_{bound} with normal pointing outwards the bounded area. Writing the position of \mathcal{P}^* as $\mathbf{p}^* \in \mathcal{W}$, the transition stage is satisfied if

$$d_{\mathbf{p}^*, \underline{\pi}_i} \leq -b_d, \quad \forall \underline{\pi}_i \in \Pi_{\text{bound}} \quad (36)$$

$$D_{\mathbf{p}^*, \underline{\pi}_{\mathcal{A}^*}} \leq b_d^2 \quad (37)$$

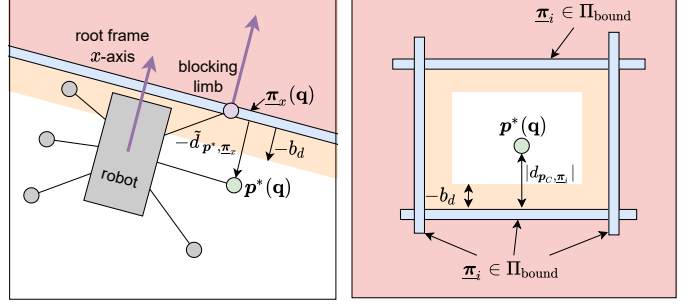


Figure 16: Illustration of the limb-crossing VFI constraint (38).
Figure 17: Illustration of the VFI constraint for respecting the bounds of \mathcal{A}^* (40).

where $d_{\mathbf{p}^*, \underline{\pi}_i}$ denotes the point-to-plane signed distance between \mathbf{p}^* and $\underline{\pi}_i$, and $D_{\mathbf{p}^*, \underline{\pi}_{\mathcal{A}^*}}$ denotes the point-to-plane square distance between \mathbf{p}^* and $\underline{\pi}_{\mathcal{A}^*}$ [16]. If conditions (36) and (37) are both already satisfied, then the transition stage is skipped.

Additionally, \mathcal{P}^* is constrained to prevent it from crossing in-front of any preceding limbs. For example, the middle-right foot of the hexapod shown in Figure 16 is prevented from crossing in-front of the front right foot (designated the *blocking limb*). Let $\underline{\pi}_x \in \mathcal{H}$ denote a plane intersecting the blocking limb's end effector with a normal vector parallel to the x -axis of the robot's root frame, which points forward with respect to the body. The signed point-to-plane distance between \mathbf{p}^* and $\underline{\pi}_x$ is written $d_{\mathbf{p}^*, \underline{\pi}_x}$, and the associated error term as $\tilde{d}_{\mathbf{p}^*, \underline{\pi}_x} \triangleq d_{\mathbf{p}^*, \underline{\pi}_x} - d_{\text{safe}, x}$ with Jacobian matrix $\mathbf{J}_{\mathbf{p}^*, \underline{\pi}_x}$ [16]. The task-space requirement is thus given as $\tilde{d}_{\mathbf{p}^*, \underline{\pi}_x} \leq -b_d$ and hence we define the VFI constraint

$$\mathbf{J}_{\mathbf{p}^*, \underline{\pi}_x} \dot{\mathbf{q}} \leq -\eta_d (\tilde{d}_{\mathbf{p}^*, \underline{\pi}_x} + b_d) + s_{\mathbf{p}^* \underline{\pi}_x}, \quad (38)$$

written in matrix/vector form as

$$\mathbf{W}_x \dot{\mathbf{q}} \preceq \mathbf{w}_x + \mathbf{s}_x. \quad (39)$$

The remaining formulations are dependent on condition (36). If condition (36) is *satisfied*, then we apply the constraint

$$\mathbf{J}_{\mathbf{p}^*, \underline{\pi}_i} \dot{\mathbf{q}} \leq -\eta_d (\tilde{d}_{\mathbf{p}^*, \underline{\pi}_i} + b_d) + s_{\mathbf{p}^* \underline{\pi}_i}, \quad \forall \underline{\pi}_i \in \Pi_{\text{bound}}, \quad (40)$$

which constrains \mathbf{p}^* to remain inside the boundaries of \mathcal{A}^* (illustrated in Figure 17). This is written in matrix/vector form as

$$\mathbf{W}_{\text{Bnd}} \dot{\mathbf{q}} \preceq \mathbf{w}_{\text{Bnd}} + \mathbf{s}_{\text{Bnd}}. \quad (41)$$

The task function is thus given as

$$\Psi_{T_1}(\dot{\mathbf{q}}) \triangleq \|\mathbf{J}_{\mathbf{p}^*, \underline{\pi}_{\mathcal{A}^*}} \dot{\mathbf{q}} + \eta_o D_{\mathbf{p}^*, \underline{\pi}_{\mathcal{A}^*}}\|_2^2, \quad (42)$$

which drives \mathbf{p}^* towards $\underline{\pi}_{\mathcal{A}^*}$, as illustrated in Figure 18.

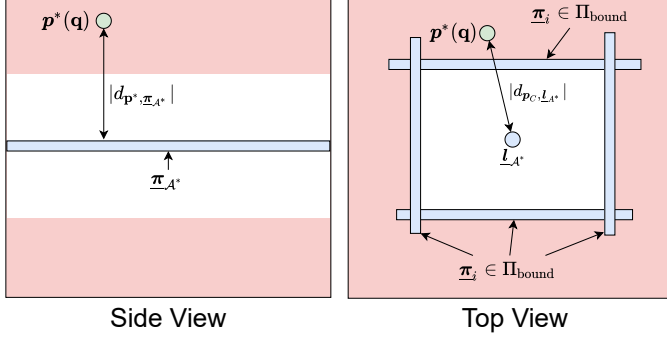


Figure 18: Illustration of transition stage task function Ψ_{T_1} , given in (42), to drive $\mathbf{p}^*(\mathbf{q})$ to the $\underline{\pi}_{A^*}$.

The complete optimisation problem is written

$$\begin{aligned} \mathbf{u} \in \operatorname{argmin}_{\dot{\mathbf{q}}, \mathbf{s}} \quad & \Psi_{T_1} + \lambda^2 \|\dot{\mathbf{q}}\|_2^2 + \beta^2 \|\mathbf{s}\|_2^2 \\ \text{subject to} \quad & \mathbf{W}_{T_1} \dot{\mathbf{q}} \preceq \mathbf{w}_{T_1} + \mathbf{s}_{T_1} \\ & \mathbf{R} \dot{\mathbf{q}} = 0 \\ & \mathbf{w}_{\min} \preceq \dot{\mathbf{q}} \preceq \mathbf{w}_{\max} \\ & \mathbf{v}_{\min} \preceq \dot{\mathbf{q}} \preceq \mathbf{v}_{\max} \\ & \mathbf{0}_\ell \preceq \mathbf{s} \preceq \mathbf{s}_{\max}, \end{aligned} \quad (43)$$

where

$$\mathbf{W}_{T_1} = \begin{bmatrix} \mathbf{W}_B \\ \mathbf{W}_x \\ \mathbf{W}_{\text{Bnd}} \end{bmatrix}, \quad \mathbf{w}_{T_1} = \begin{bmatrix} \mathbf{w}_B \\ \mathbf{w}_x \\ \mathbf{w}_{\text{Bnd}} \end{bmatrix}, \quad \mathbf{s}_{T_1} = \begin{bmatrix} \mathbf{s}_B \\ \mathbf{s}_x \\ \mathbf{s}_{\text{Bnd}} \end{bmatrix},$$

with \mathbf{W}_B given in 35.

In this stage, the balance constraint (24) is defined using the region Π_{without} and the contact slippage constraint (26) uses $\mathcal{R}_{\text{fixed}} = \mathcal{R} \setminus \{\mathcal{P}^*\}$.

Alternatively, if condition (36) is *not satisfied*, then constraint (40) is not applied and a new task function is written

$$\Psi_{T_2}(\dot{\mathbf{q}}) \triangleq \left\| \mathbf{J}_{\mathbf{p}^*, \underline{L}_{A^*}} \dot{\mathbf{q}} + \eta_o \tilde{D}_{\mathbf{p}^*, \underline{L}_{A^*}} \right\|_2^2, \quad (44)$$

where $\underline{L}_{A^*} \in \mathcal{H}_p \cap \mathcal{S}$ is a line perpendicular to the contact plane intersecting its centroid, similar to that in (33). Thus this additional task function brings \mathbf{p}^* into the region described by Π_{bound} , as illustrated in Figure 19. The problem is hence re-written to include *both* task functions

$$\begin{aligned} \mathbf{u} \in \operatorname{argmin}_{\dot{\mathbf{q}}, \mathbf{s}} \quad & \Psi_{T_2} + \Psi_{T_1} + \lambda^2 \|\dot{\mathbf{q}}\|_2^2 + \beta^2 \|\mathbf{s}\|_2^2 \\ \text{subject to} \quad & \mathbf{W}_{T_2} \dot{\mathbf{q}} \preceq \mathbf{w}_{T_2} + \mathbf{s}_{T_2} \\ & \mathbf{R} \dot{\mathbf{q}} = 0 \\ & \mathbf{w}_{\min} \preceq \dot{\mathbf{q}} \preceq \mathbf{w}_{\max} \\ & \mathbf{v}_{\min} \preceq \dot{\mathbf{q}} \preceq \mathbf{v}_{\max} \\ & \mathbf{0}_\ell \preceq \mathbf{s} \preceq \mathbf{s}_{\max}, \end{aligned} \quad (45)$$

where

$$\mathbf{W}_{T_2} = \begin{bmatrix} \mathbf{W}_B \\ \mathbf{W}_x \end{bmatrix}, \quad \mathbf{w}_{T_2} = \begin{bmatrix} \mathbf{w}_B \\ \mathbf{w}_x \end{bmatrix}, \quad \mathbf{s}_{T_2} = \begin{bmatrix} \mathbf{s}_B \\ \mathbf{s}_x \end{bmatrix}.$$

As in the breaking stage, either problem (43) or (45) is solved (as appropriate) and numerical integration is used to find the next configuration. Once conditions (36) and (37) are both satisfied, the transition stage terminates and the posture generator progresses to the placement optimisation stage. If either condition is not satisfied, then the process repeats, returning a failure state if a user-defined maximum number of integration step cycles is reached.

5.2.4. Placement Optimisation Stage

Finally, in the placement optimisation stage the posture generator optimises the position of the new contact with respect to the potential field $U(\mathbf{q})$, given in (51). Since only the contact patch \mathcal{P}^* is free to move in this stage, only the contact patch-specific sub-field $U_{\mathcal{P}^*}(\mathbf{q})$, given by (10), is relevant to this optimisation, since the other sub-terms remain constant. The time derivative of $U_{\mathcal{P}^*}(\mathbf{q})$ is given by

$$\frac{d}{dt} U_{\mathcal{P}^*}(\mathbf{q}) = \dot{D}_{\mathbf{p}^*, \underline{L}_{*, \min}} + \alpha \dot{D}_{\mathbf{p}^*, \underline{\pi}_{*, \min}}, \quad (46)$$

where $D_{\mathbf{p}^*, \underline{L}_{*, \min}}$ and $D_{\mathbf{p}^*, \underline{\pi}_{*, \min}}$ have the same meanings as in (10). The Jacobian matrix of $U_{\mathcal{P}^*}(\mathbf{q})$ (denoted $\mathbf{J}_{U_{\mathcal{P}^*}}$) is straightforwardly defined by writing

$$\dot{D}_{\mathbf{p}^*, \underline{L}_{*, \min}} + \alpha \dot{D}_{\mathbf{p}^*, \underline{\pi}_{*, \min}} = \underbrace{\left(\mathbf{J}_{\mathbf{p}^*, \underline{L}_{*, \min}} + \alpha \mathbf{J}_{\mathbf{p}^*, \underline{\pi}_{*, \min}} \right)}_{\mathbf{J}_{U_{\mathcal{P}^*}}} \dot{\mathbf{q}}. \quad (47)$$

With this, the task function for the placement optimisation stage is given as

$$\Psi_O(\dot{\mathbf{q}}) = \|\mathbf{J}_{U_{\mathcal{P}^*}} \dot{\mathbf{q}} + \eta_o U_{\mathcal{P}^*}(\mathbf{q})\|_2^2, \quad (48)$$

which drives the robot to move contact patch \mathcal{P}^* to a position that minimises $U_{\mathcal{P}^*}(\mathbf{q})$ and, consequently, $U(\mathbf{q})$.

Finally, we limit the maximum square distance from \mathbf{p}^* to $\underline{\pi}_{A^*}$ (illustrated in Figure 20) by applying the constraint

$$\mathbf{J}_{\mathbf{p}^*, \underline{\pi}_{A^*}} \dot{\mathbf{q}} \leq -\eta_d (D_{\mathbf{p}^*, \underline{\pi}_{A^*}} + b_d^2) + s_{\mathbf{p}^*, \underline{\pi}_{A^*}}, \quad (49)$$

written in matrix/vector form as

$$\mathbf{W}_{A^*} \dot{\mathbf{q}} \preceq \mathbf{w}_{A^*} + \mathbf{s}_{A^*}.$$

The complete optimisation problem can thus be written as

$$\begin{aligned} \mathbf{u} \in \operatorname{argmin}_{\dot{\mathbf{q}}, \mathbf{s}} \quad & \Psi_O + \lambda^2 \|\dot{\mathbf{q}}\|_2^2 + \beta^2 \|\mathbf{s}\|_2^2 \\ \text{subject to} \quad & \mathbf{W}_O \dot{\mathbf{q}} \preceq \mathbf{w}_O + \mathbf{s}_O \\ & \mathbf{R} \dot{\mathbf{q}} = 0 \\ & \mathbf{w}_{\min} \preceq \dot{\mathbf{q}} \preceq \mathbf{w}_{\max} \\ & \mathbf{v}_{\min} \preceq \dot{\mathbf{q}} \preceq \mathbf{v}_{\max} \\ & \mathbf{0}_\ell \preceq \mathbf{s} \preceq \mathbf{s}_{\max}, \end{aligned} \quad (50)$$

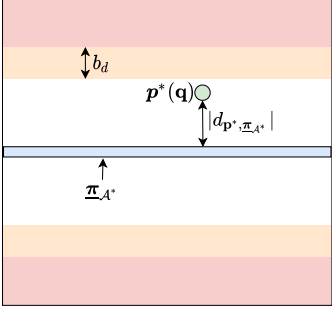


Figure 20: Illustration of the VFI constraint (49) for keeping \mathcal{P}^* close to \mathcal{A}^* while its location is optimised.

where

$$\mathbf{W}_O = \begin{bmatrix} \mathbf{W}_{T_1} \\ \mathbf{W}_{\mathcal{A}^*} \end{bmatrix}, \mathbf{w}_O = \begin{bmatrix} \mathbf{w}_{T_1} \\ \mathbf{w}_{\mathcal{A}^*} \end{bmatrix}, \mathbf{s}_O = \begin{bmatrix} \mathbf{s}_{T_1} \\ \mathbf{s}_{\mathcal{A}^*} \end{bmatrix}.$$

As in the transition stage, the balance constraint (24) is defined using the region Π_{without} and the contact slippage constraint (26) uses $\mathcal{R}_{\text{fixed}} = \mathcal{R} \setminus \{\mathcal{P}^*\}$.

Also like the previous stages, problem (50) is solved and numerical integration is used to find the next configuration. If $\mathbf{u} \approx \mathbf{0}$, then the placement optimisation stage terminates and the posture generation process is complete. Alternatively, if $\mathbf{u} \not\approx \mathbf{0}$, then the process repeats. If the user-defined maximum number of integration step cycles is reached, then the process terminates and the most recent iterate is returned.

6. Contact-critical Local Minima

This section discusses contact-critical local minima (CLM) problems that might affect CBM planners that rely on potential-field-based guide paths. The causes of these local minima are examined, and heuristics are developed to mitigate them.

6.1. Causes of Local Minima

CLM are a form of local minima that coincide with the confluence of the following three conditions:

- **Condition 1** - The robot cannot meaningfully progress without breaking a particular contact, denoted $c^* = (\mathcal{P}^*, \mathcal{A}^*, \mathbf{p}^{\mathcal{A}^*})$. This most often occurs when the other contact patches have each been moved from their previous position and cannot be moved much further until \mathcal{P}^* is also moved.
- **Condition 2** - The contact c^* is critical to the robot's balance, meaning that if c^* were broken in the current configuration, then the robot would fall. Thus, in order to safely break contact c^* , the robot must first move its centre of mass (COM) to a region where c^* is not required for balance. A horizontal cross-section of this region for a hexapod robot in the configuration shown in Figure 21 is shown in red in Figure 22.

- **Condition 3** - The robot cannot move its COM into the required region without breaking contact c^* first. An approximation of the reachable area for the robot torso (which typically contains the COM) is shown in green in Figure 22. Since there is no overlap between the green region and the red polygon in Figure 22, the robot cannot reach a configuration from which foot 3 can be safely lifted.

Figure 23 shows examples of the robot during CLM in various scenarios. In principle, the robot could escape from CLM by moving another limb to relieve contact c^* , making it no-longer critical for balance. However, the potential fields that guide CBM planners, such as CVBFP and RHCP, strongly disincentivise moving contact patches away from the goal [4]. Thus, the algorithm's respective posture generators rarely form contacts that can relieve c^* , and when they do their search algorithms will not typically choose to expand these nodes. Hence, escaping from CLM can be very difficult for both planners.

While trapped in a CLM, the planning processes may generate very large quantities of nodes descending from the 'stuck' position, exploring many different future step sequences, none of which result in significant forward movement, since meaningful progress remains impossible without breaking contact c^* . This typically continues until the planners become unable to generate any more nodes descending from the stuck position and are forced to retreat to a prior state. Other avenues may then be explored in which contact c^* can be broken, allowing progress to resume. Both planners prevent duplicate positions from being repeated, guaranteeing that they will both break out of CLM after a finite time. However, in practice this may take too long.

CLM-causing configurations are favoured by search processes, despite their deleterious impacts, because the potential fields guiding CBM planners incentivise the robot to move its limbs forward, with larger steps being preferred. The front legs of the Corin hexapod, for example, typically have more space to move than others, meaning that the front legs often move first, followed by the middle legs and finally the rear legs. This increases the likelihood that one rear leg will become critical for balance and unable to be safely lifted.

6.2. Improving Resilience

In response to the problems posed by CLM, we make two changes to the basic RHCP shown in Figure 2. First, the potential field is reformulated to discourage the robot from entering positions resembling those shown in Figure 23. Second, we add a heuristic mechanism that detects the presence of CLM and takes corrective action to escape. These measures were chosen because they do not disallow any configurations that were previously permitted, meaning that the planner is not made any more conservative.

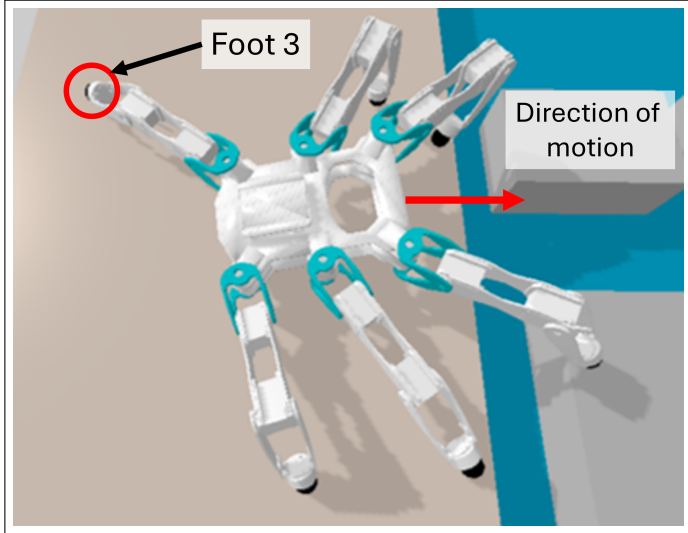


Figure 21: The Corin hexapod during a CLM.

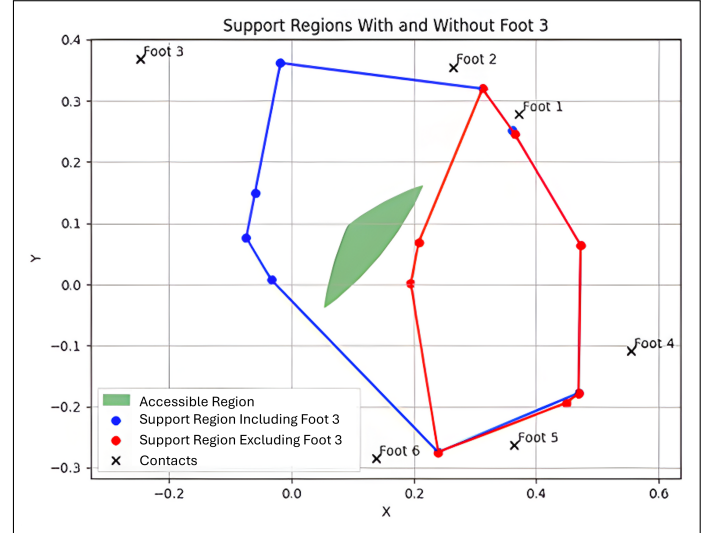
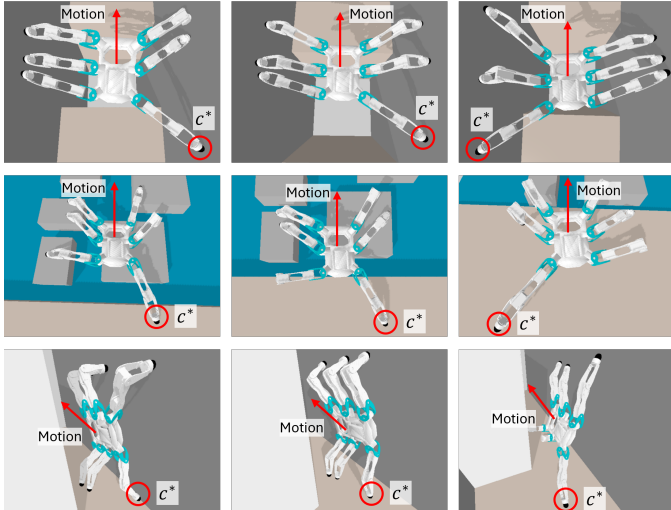


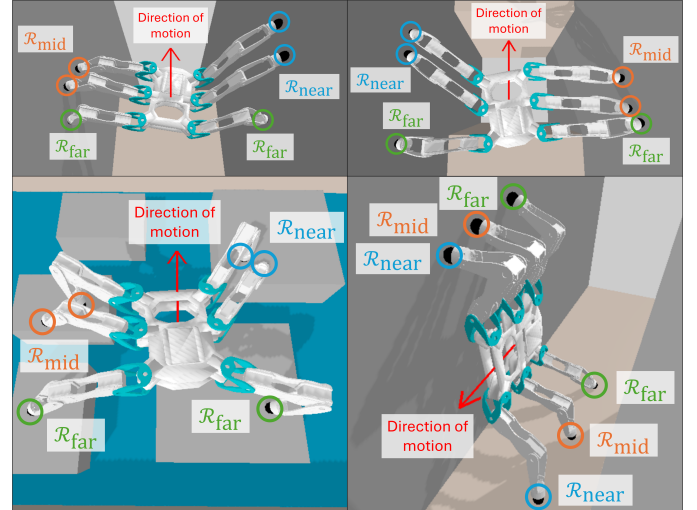
Figure 22: The support regions with (blue) and without (red) the rear left foot (foot 3) for the Corin hexapod in the configuration shown in Figure 21.

Figure 23: Examples of the Corin hexapod during contact-critical local minima. In each case, contact c^* is indicated by a red circle, and the direction of motion by the red arrow.

6.2.1. Encouraging Movement of Farthest Legs

To discourage the robot from taking on configurations resembling those in Figure 23, the potential field is reformulated such that movements of the feet that are farthest away from the end position are prioritised over those closer to the end position.

Let the point $\mathbf{p}_{s_G} \in \mathcal{W}$ be the mean 3D location of all of the contacts comprising the goal stance s_G . When the potential is determined for a configuration \mathbf{q} , each of the robot's contact patches $\mathcal{P} \in \mathcal{R}$ are automatically assigned to one of three sets based on their distance from \mathbf{p}_{s_G} . The nearest two patches are assigned to $\mathcal{R}_{\text{near}}$, the furthest two to \mathcal{R}_{far} , and the remaining two to \mathcal{R}_{mid} . Figure 24 shows examples of configurations in different scenarios with their

Figure 24: Example configurations in different scenarios with the contacts assigned to either $\mathcal{R}_{\text{near}}$, \mathcal{R}_{mid} , or \mathcal{R}_{far} .

contacts assigned to these sets.

The revised potential field is then given as

$$U(\mathbf{q}) = \sum_{i=1}^{n_{\mathcal{R}}} \beta_i U_{\mathcal{P}_i}(\mathbf{q}), \quad (51)$$

where $\beta_i \in (0, 2)$ is determined based on the set to which the contact patch \mathcal{P}_i belongs,

$$\beta_i = \begin{cases} 1 - b & \text{if } \mathcal{P}_i \in \mathcal{R}_{\text{near}} \\ 1 & \text{if } \mathcal{P}_i \in \mathcal{R}_{\text{mid}} \\ 1 + b & \text{if } \mathcal{P}_i \in \mathcal{R}_{\text{far}}, \end{cases} \quad (52)$$

where $b \in [0, 1)$. The term $U_{\mathcal{P}_i}(\mathbf{q})$ is calculated as given in (10).

This change causes the search process to prioritise the limbs that are the furthest away from the goal stance before moving those closest. This causes the planning process to disfavour moves that will result in stuck positions like those shown in Figure 23.

One drawback of this approach is that the contact patches of different robots must be sorted into sets differently depending on their geometries. For example, a quadruped may assign the two closest patches to $\mathcal{R}_{\text{near}}$, the two farthest to \mathcal{R}_{far} , and leave \mathcal{R}_{mid} empty. Likewise, a humanoid may allocate one patch each to $\mathcal{R}_{\text{near}}$ and \mathcal{R}_{far} . This need to specify how patches should be allocated for different robot geometries somewhat reduces the generality of the approach, but these adaptations are judged unlikely to pose a significant obstacle to generalisation in most cases.

6.2.2. Intervention Mechanism

Though the revised potential field makes CLM issues *less likely* to occur, it does not prevent them entirely. Therefore, we also design a heuristic intervention mechanism that detects CLM and takes corrective action to break out. The mechanism is triggered if either of two conditions are met:

1. There exists a contact c^* that has been impossible to break safely in all of the $\gamma \in \mathbb{N}$ most recently occupied root nodes.
2. The planning process has encountered a dead end (*i.e.*, $\mathcal{G}_{\kappa_{\max}} = \emptyset$) *and* there exists a contact c^* that cannot be safely broken from the current root node.

When the mechanism is triggered, it takes corrective action to break the search process out of the local minimum (illustrated in Figure 25). This begins with the robot retreating to the previous state (the parent node of the current root node). When the robot has arrived in that state, it is redesignated \mathbf{n}_0 and becomes the new root node. The child generation process is done by restoring child nodes from a global cache, denoted \mathcal{C}_G in Figure 25, until generation $\mathcal{G}_{\kappa_{\max}}$ is reached.

As each generation of child nodes is restored, any nodes that have previously been the root node are purged from the set. This prevents the system from repeating previous stances that are known to be ineffective.

Once $\kappa = \kappa_{\max}$, the nodes comprising $\mathcal{G}_{\kappa_{\max}}$ are each checked in order to determine whether contact patch \mathcal{P}^* has moved to a different location, thus breaking contact c^* . Any nodes that meet this condition are added to a set of ‘escape nodes’ denoted $\mathcal{G}_{\text{esc}} \subset \mathcal{G}_{\kappa_{\max}}$. The lowest-potential node in \mathcal{G}_{esc} , designated \mathbf{n}_{esc} , is then identified and the sequence of nodes leading from \mathbf{n}_0 to \mathbf{n}_{esc} is designated \mathcal{N}_{esc} . The robot then performs the series of motions required to execute the sequence \mathcal{N}_{esc} , arriving at \mathbf{n}_{esc} , which becomes the new root node. The nodes in \mathcal{N}_{esc} are hence added to the root cache \mathcal{C}_R , and planning resumes as normal.

If no valid escape nodes can be found (*i.e.*, $\mathcal{G}_{\text{esc}} = \emptyset$), then the robot retreats again to the parent node of \mathbf{n}_0 and

repeats the process. This continues until either a valid escape node is found, or the process has backed up to the initial state \mathbf{n}_I (which has no parent node) at which point the planning is considered to have failed. An updated flowchart displaying the revised algorithm is shown in Figure 26.

7. Configuration Update by Numerical Integration With Contact Drift Correction

Once a control input \mathbf{u} is generated by solving the optimisation problems (34) (breaking stage), (43) (transition stage), (45) (transition stage when (37) is not satisfied), or (50) (placement optimisation), the robot configuration is updated via numerical integration. First, the configuration velocity vector,

$$\dot{\mathbf{q}} \triangleq [\text{vec}_4(\dot{\mathbf{r}}(t)) \quad \text{vec}_3(\dot{\mathbf{p}}(t)) \quad \dot{\boldsymbol{\theta}}(t)]^T,$$

is extracted from $\mathbf{u} = (\dot{\mathbf{q}}, \mathbf{s})$, and the torso pose derivative is calculated as

$$\dot{\underline{\mathbf{x}}}(t) = \dot{\mathbf{r}}(t) + \varepsilon \frac{1}{2} (\dot{\mathbf{p}}(t)\mathbf{r}(t) + \mathbf{p}(t)\dot{\mathbf{r}}(t)). \quad (53)$$

Then, the next torso pose $\underline{\mathbf{x}}(t + \tau)$ and joint angle vector $\boldsymbol{\theta}(t + \tau)$, where $\tau \in (0, \infty]$ is the integration step, are calculated as

$$\underline{\mathbf{x}}(t + \tau) = \exp(\tau \dot{\underline{\mathbf{x}}}(t) \underline{\mathbf{x}}(t)^*) \underline{\mathbf{x}}(t), \quad (54)$$

$$\boldsymbol{\theta}(t + \tau) = \boldsymbol{\theta}(t) + \tau \dot{\boldsymbol{\theta}}(t), \quad (55)$$

where the (dual quaternion) exponential map and group operation in (54) ensures that the underlying topology of unit dual quaternions is respected [15]. The pose $\underline{\mathbf{x}}(t + \tau)$ can hence be decomposed into $\mathbf{r}(t + \tau)$ and $\mathbf{p}(t + \tau)$, and used to form the overall configuration

$$\mathbf{q}(t + \tau) \triangleq [\text{vec}_4(\mathbf{r}(t + \tau)) \quad \text{vec}_3(\mathbf{p}(t + \tau)) \quad \boldsymbol{\theta}(t + \tau)]^T. \quad (56)$$

7.1. Contact drift correction

As discussed in Section 5.1, discrete integration steps can cause robot bodies to enter restricted zones, which we partially resolve with the addition of constraint buffers. However, the relatively small safe zone of the contact sliding constraint (26), coupled with relatively large integration step sizes, causes two problems:

1. To guarantee that the next configuration will remain within the safe zone, the size of the buffer region would need to be greater than the radius of the safe zone itself (*i.e.*, $b_d > R_{\text{slip}}$ in Figure 13), making satisfying the requirement that $D_{\mathbf{p}_i, \mathbf{p}_{d_i}} - R_{\text{slip}}^2 \leq -b_d^2$ impossible.

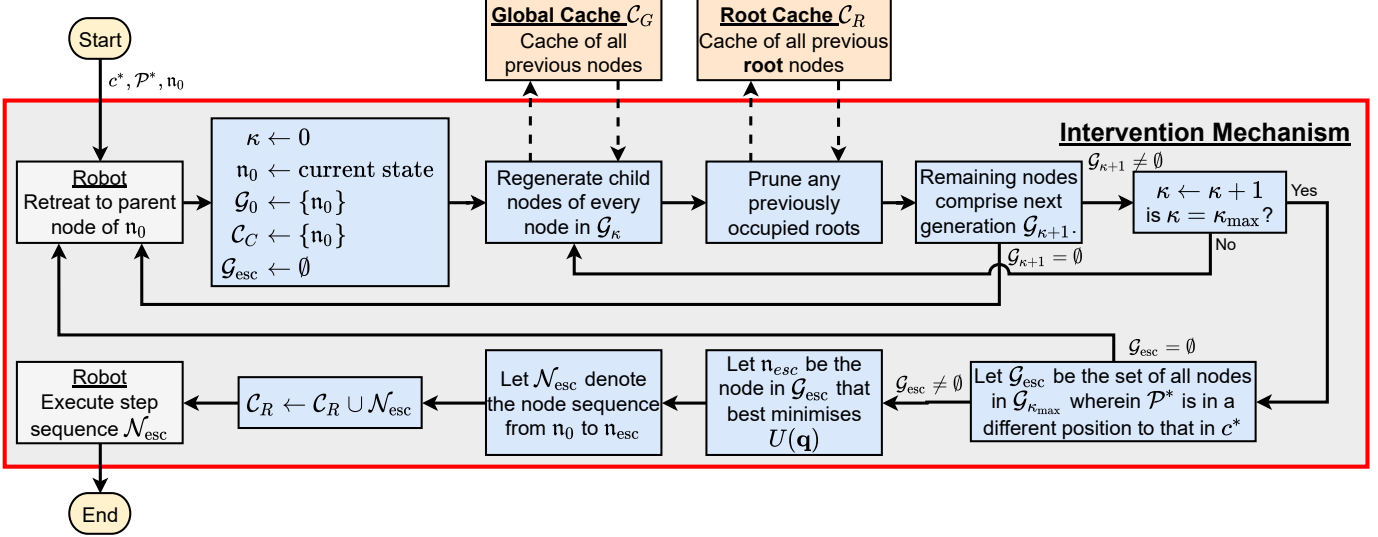


Figure 25: Flowchart illustrating the intervention mechanism that mitigates CLM.

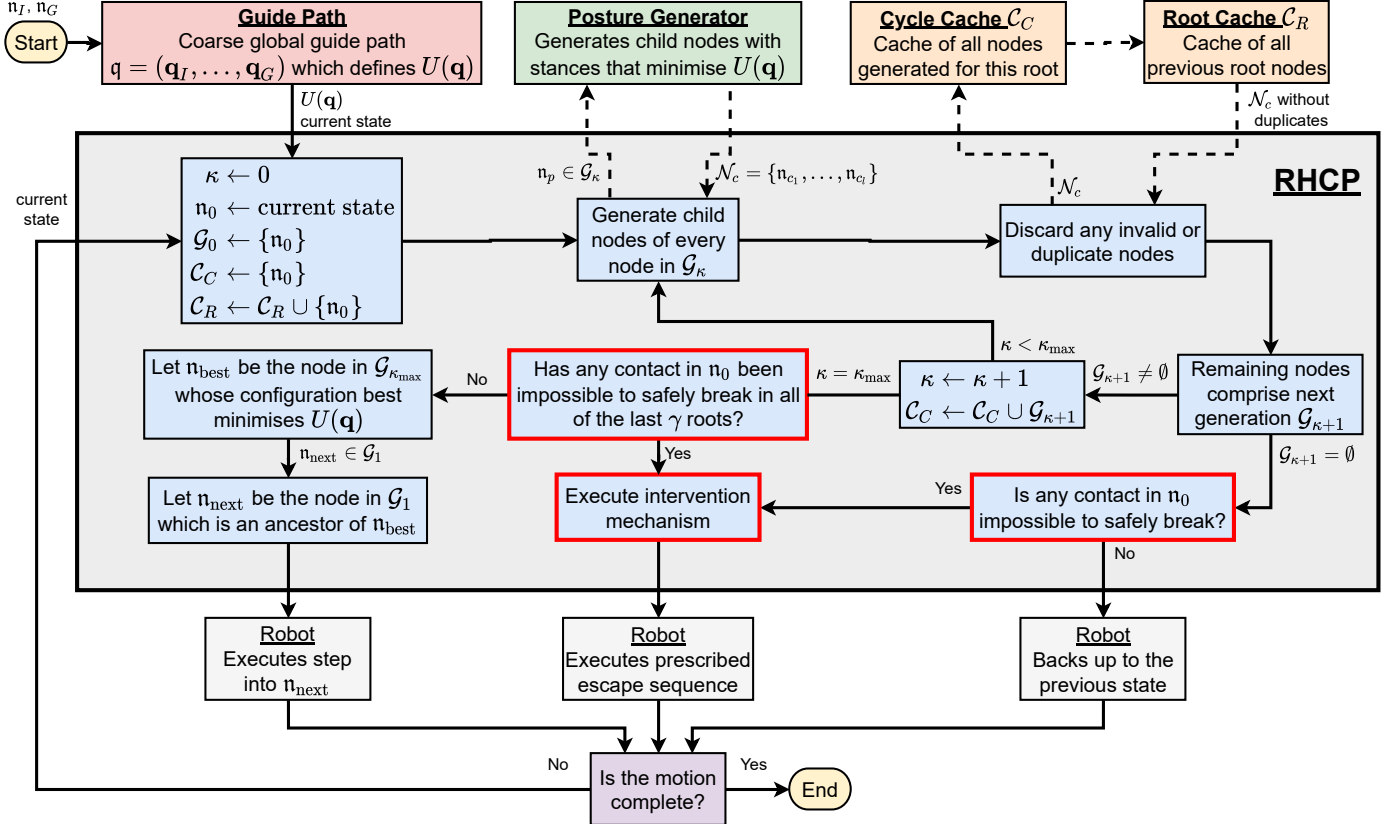


Figure 26: Updated flowchart illustrating the RHCP planning algorithm with the improvements, highlighted in red, to mitigate CLM: an improved potential-field guide-path and an intervention mechanism that finds escape nodes.

2. Constraint (26) limits how fast \mathbf{p}_i may approach the *edge* of the safe zone, but the velocity of \mathbf{p}_i towards the *centre* of the zone is not restricted. Since the spherical safe zone is very small, \mathbf{p}_i may pass the centre of the zone with sufficient speed to cross the boundary on the other side, due to discretisation,

before the antipodal point's VFI starts having an effect.

These problems may be mitigated by using smaller integration steps, however, this would mean more control cycles are necessary to plan the same motion, directly increasing the execution time of the planner. Instead, if any con-

tact patch $\mathcal{P}_i \in \mathcal{R}_{\text{fixed}}$ has drifted too far from its desired location, and hence violated the constraint, a secondary constrained controller corrects the drift.

We define $\mathbf{D}_{\text{drift}}$ as the stacked vector of square distances between each fixed contact patch and its desired location, given by

$$\mathbf{D}_{\text{drift}} \triangleq \begin{bmatrix} D_{\mathbf{p}_1, \mathbf{p}_{d,1}} \\ \vdots \\ D_{\mathbf{p}_n, \mathbf{p}_{d,n}} \end{bmatrix}, \forall \mathcal{P}_i \in \mathcal{R}_{\text{fixed}}.$$

Writing the Jacobian matrix of $\mathbf{D}_{\text{drift}}$ as $\mathbf{J}_{\text{drift}} = \partial \mathbf{D}_{\text{drift}} / \partial \mathbf{q}$, we hence design the drift-correction controller as

$$\begin{aligned} \mathbf{u} \in \underset{\dot{\mathbf{q}}}{\operatorname{argmin}} \quad & \|\mathbf{J}_{\text{drift}} \dot{\mathbf{q}} + \eta_o \mathbf{D}_{\text{drift}}\|_2^2 + \lambda^2 \|\dot{\mathbf{q}}\|_2^2 \\ \text{subject to} \quad & \mathbf{R} \dot{\mathbf{q}} = 0 \\ & \mathbf{w}_{\min} \preceq \dot{\mathbf{q}} \preceq \mathbf{w}_{\max} \\ & \mathbf{v}_{\min} \preceq \dot{\mathbf{q}} \preceq \mathbf{v}_{\max}, \end{aligned} \quad (57)$$

where $\mathbf{R}, \mathbf{w}_{\min}, \mathbf{w}_{\max}$ are defined in Section 5.2.

7.2. Variable integration step sizes

Drift correction reduces the frequency of contact sliding. However, relatively small values of τ remain necessary to avoid violating other constraints (or else using very conservative buffers). We resolve this by varying τ between τ_{\min} and τ_{\max} , making large steps where possible and smaller steps where necessary.

Whenever a value of \mathbf{u} is returned, $\mathbf{q}(t+\tau)$ is calculated using (56) with $\tau = \tau_{\max}$. Any contact drifts are corrected, and the resulting configuration is checked to verify that the constraints are satisfied. If so, then the posture generator progresses to the next optimisation. If, however, $\mathbf{q}(t+\tau)$ is *invalid* (i.e., any safety critical constraint are violated when robot is at configuration $\mathbf{q}(t+\tau)$), then τ is decremented by $\Delta\tau$ and $\mathbf{q}(t+\tau)$ is recalculated. This continues until either a valid step is found or $\tau \leq \tau_{\min}$, in which case the posture generator terminates and returns a failure. A flowchart for this process is provided in Figure 27.

8. Planning Simulations and Statistical Evaluation

8.1. Experimental Setup

The RHCP planning framework was compared to CVBFP in the four simulated scenarios depicted in Figure 28. Each scenario requires different forms of motion to be planned for the Corin hexapod. In the Wall Walking scenario, the robot moves through a narrow one-meter corridor by forming contacts on a vertical wall. In the Chimney Walking scenario, the robot crosses a one-meter gap in the ground by using the vertical surfaces exclusively. In the Chimney Climbing case, the robot vertically climbs a one-meter-tall chimney. In the Stepping Stones environment, the robot crosses a two-meter-wide ‘river’ using sparse, non-repeating surfaces. An animation of the robot executing an

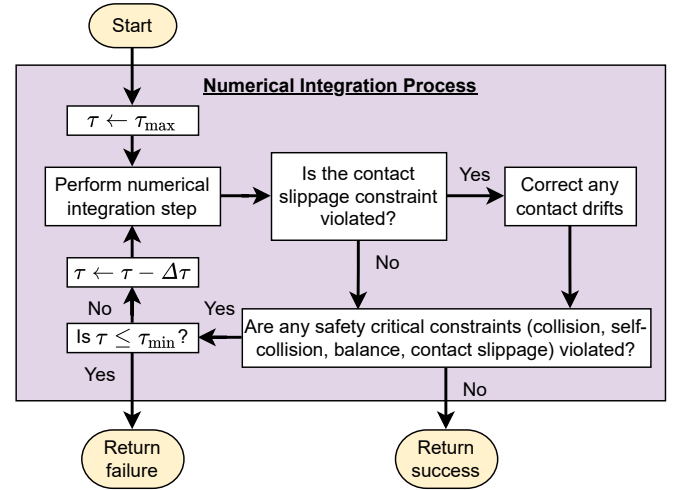


Figure 27: Flowchart of the numerical integration process with variable integration step sizes.

example motion plan (generated by RHCP with $\kappa_{\max} = 2$) in each scenario is available in the supplementary video for this article. Snapshots of a motion plan in the Stepping Stones scenario are also shown in Figure 29.

Both planners generated motion plans for the Corin hexapod [13] in each scenario from partially randomised starting configurations. RHCP used a variety of horizon depths for the tests, varying from $\kappa_{\max} = 1$ to $\kappa_{\max} = 4$. CVBFP, and RHCP with $\kappa_{\max} \in \{1, 2, 3\}$, each generated 100 motion plans per scenario. Due to the large planning times required, only 50 motion plans were generated for RHCP with $\kappa_{\max} = 4$.

The total time required to plan each motion was recorded, as well as the number of total stance changes required to execute the resulting motion plan. Note that lifting and then placing a foot is counted as two separate stance changes. All tests were run in a computer running Ubuntu 20.04.6 LTS (64 bits) with an Intel® Core™ i9-7900X Processor and 62 GB RAM. Posture generator calls were batched and made concurrently with a maximum of 20 threads. For CVBFP, all children/siblings of a given node were generated in one batch, whereas in RHCP all nodes in a given generation formed one batch. Both posture generators were written in C++ and both the tree search methods were written in Python. Where objects in the environment were modelled by dual quaternion primitives, the kinematic calculations were handled by the DQ Robotics C++ library [22]. Otherwise, the simulator Bullet was used, accessed via its fast C++ interface [23].

This experimental set-up is very similar to that in our previous work [14], though with some important differences. One difference is that here we analyse multiple horizon depths, whereas in [14] only a two-step horizon (i.e., $\kappa_{\max} = 2$) was considered. Additionally, in [14] the balance criterion of CVBFP was implemented as described in [4], with no upper bound on the magnitudes of the contact forces. This was also the case for RHCP’s balance

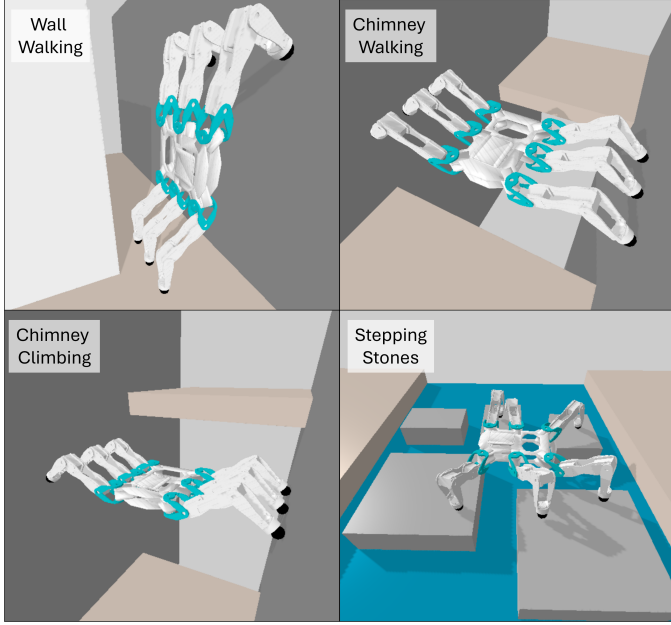


Figure 28: Testing scenarios used for experimentation, referred to as Wall Walking (top left), Chimney Walking (top right), Chimney Climbing (bottom left) and Stepping Stones (bottom right).

criterion, described in [20]. The effect of this is that CLM posed a much smaller problem for both planners in [14] than they do in this present work, which is more realistic, and hence the experimental results in this present work are more insightful and physically plausible than those given in [14].

8.2. Statistical Evaluation

Bayesian analysis techniques were used to inform a probabilistic model of the performance of each planner with respect to each metric in each environment [24]. Raw data distributions for tests that encountered a large number of CLM often showed two distinct peaks, one for when CLM occur and one for when they do not. Therefore, we model each metric as a bimodal t -distribution [25], written as

$$m \sim w_A t_A(\mu_A, \rho_A, \nu_A) + w_B t_B(\mu_B, \rho_B, \nu_B), \quad (58)$$

where μ_A and μ_B denote the means of components A and B respectively. Likewise, ρ_A and ρ_B denote the components' respective scale parameters, whereas ν_A and ν_B denote their respective normality parameters (also called degrees of freedom). The two components are weighted by the terms $w_A \in [0, 1]$ and $w_B \triangleq 1 - w_A$. If the median posterior estimate for either weighting is above 0.9 in a given model, then that model is considered *effectively* unimodal and the less-weighted component is excluded from the results. This is because, in such cases, the less-weighted component has little impact on the posterior probabilities, and thus its parameters may fail to converge to estimates informed by the data. Therefore, analysing such parameter estimates is of little value.

Table 1: Prior distributions used for the parameters of model (58).

Parameter	Prior Distribution
Means μ_A, μ_B	Normal ($\mu = M_m, \sigma = 100S_m$)
Scales ρ_A, ρ_B	Uniform ($L = \frac{S_m}{1000}, H = 1000S_m$)
Normalities ν_A, ν_B	Exponential ($\lambda = 30$)
Weighting w_A	Uniform ($L = 0, H = 1$)

The priors used for each model parameter are given in Table 1, and describe broad distributions based on the sample mean M_m and sample standard deviation S_m of the dataset, reflecting little pre-existing knowledge about how the algorithms would compare.

For each combination of metric, horizon depth, and scenario, we present the probability distributions describing the most credible range of mean performance differences between CVBFP and RHCP (planning times in Figure 30 and number of stance changes in Figure 31). These differences are given in the form $\mu_{\text{RHCP}} - \mu_{\text{CVBFP}}$, meaning that a negative result indicates that RHCP exhibits a reduction in this metric with respect to CVBFP, and vice versa.

The most credible range of estimates for the mean difference, given the data, is described by the 95% Highest Density Interval (HDI) of each posterior distribution (indicated by the *black* horizontal bars on each distribution in Figures 30 and 31). This is the range that contains 95% of the probability density, such that all estimates within the range are more credible than all estimates outside the range. Thus, there is a 95% chance that the *true* mean difference lies within this range. The median estimate is also shown in Figures 30 and 31 by the *green* horizontal bar for each distribution.

The red dashed lines in Figures 30 and 31 denote the Region of Practical Equivalence (ROPE), defined as the range of differences too small to be considered practically meaningful for our purposes. For the planning time comparisons, we chose a ROPE equal to $\pm 10\%$ of the median planning time for CVBFP in that scenario. For the number of stance changes, we chose $\pm 5\%$ of the number of stance changes that CVBFP would be expected to make if it took the smallest allowable step in our implementation (10 cm). For example, in a one-metre-long scenario a six-legged robot making 10 cm steps would need to execute 60 steps, or 120 stance changes. Hence, a ROPE of ± 6 stance changes is used in such a case.

If the 95% HDI of a given distribution overlaps the ROPE, then there is a credible possibility that the true difference is not practically meaningful. Thus, we cannot be confident that a practical difference exists in these cases. Alternatively, if the 95% HDI does not overlap with the ROPE, then we can be confident that a practically meaningful difference exists.

A two-hour maximum time limit was imposed on each test. A total of 34 out of 100 motion planning attempts by

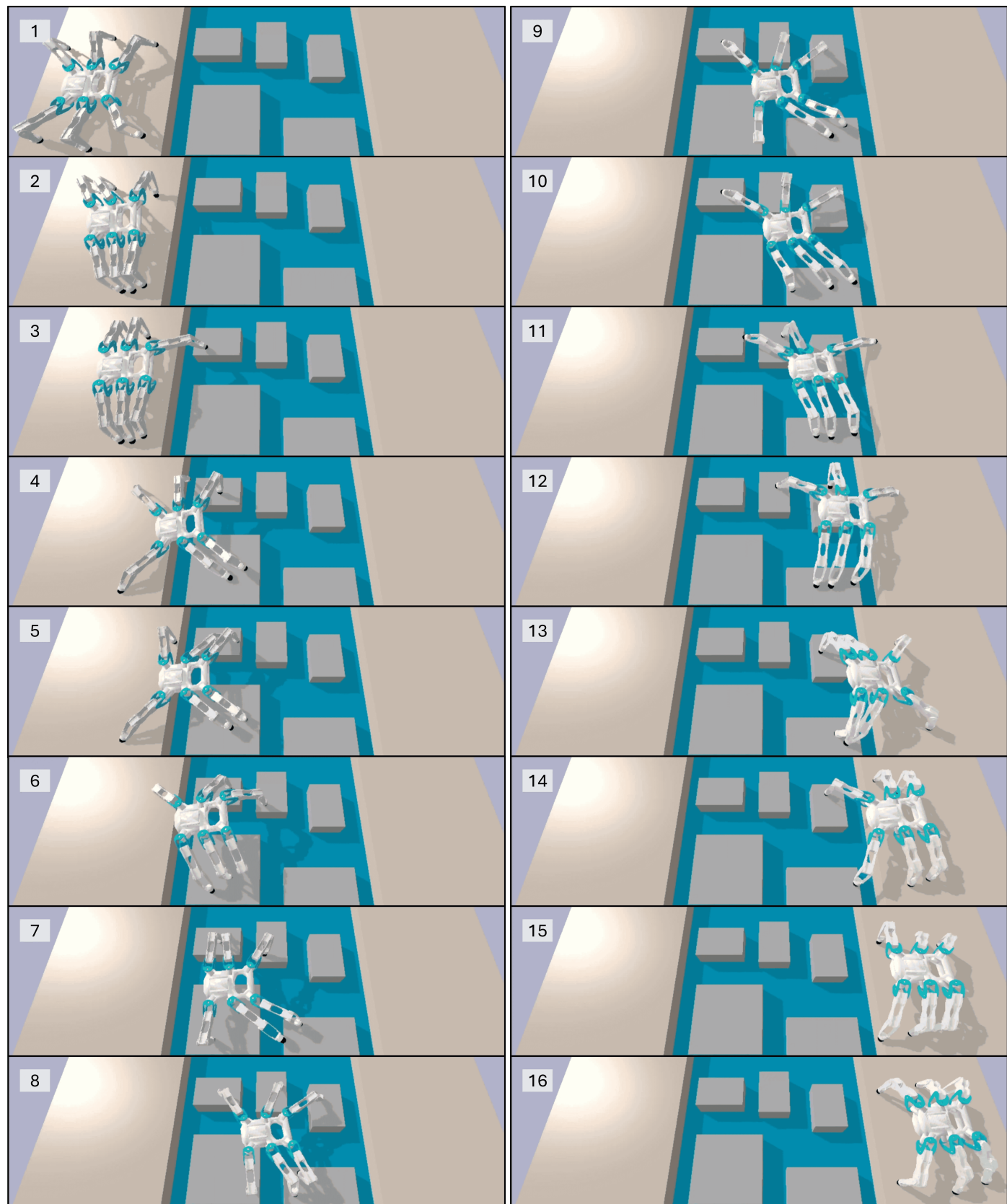


Figure 29: Snapshots of a motion plan generated by RHCP in the Stepping Stones scenario.

CVBFP in the Wall Walking scenario exceeded the time limit and were terminated. Therefore, the data from these tests are excluded from the analysis in this section. Additionally, one out 100 RHCP motion planning attempt (when $\kappa_{\max} = 1$, also in the Wall Walking environment) failed to return a motion plan due to the planner's lack of completeness (mentioned in Section 3.1). All other planning attempts concluded successfully and without issue.

8.2.1. Planning time

As expected, Figure 30 shows that longer horizon depths result in longer planning times. Indeed, the distributions display an approximately exponential curve with respect to horizon depth in most cases, in line with expectations given by expression (6).

Figure 30 also shows that, when $\kappa_{\max} = 1$, RHCP executes meaningfully faster than CVBFP across all scenarios, with the median time saving ranging from 2.6 minutes in the Chimney Climbing scenario (component B) to 66.8 minutes in the Wall Walking scenario (component A). This is also true in most cases when $\kappa_{\max} = 2$ (as was our finding in [14]), with the exception of component B in the Stepping Stones scenario, whose 95% HDI spans the ROPE. Thus, in this case it is not possible to be confident in the true mean difference, with an increase, a decrease or no practical difference with respect to CVBFP all being credible possibilities. We note, however, that the weighting of component B in this case is approximately 0.18, meaning that an individual motion plan is most likely to belong to component A, whose mean planning time is meaningfully faster than CVBFP's (3.9 minutes faster).

For longer horizons ($\kappa_{\max} > 2$), the planning time comparisons are more mixed and depend on the scenario. In the Chimney Climbing and Stepping Stones scenarios, RHCP with $\kappa_{\max} = 3$ has a meaningfully slower mean execution time than CVBFP (1.7 minutes and 10 minutes slower, respectively), as does RHCP with $\kappa_{\max} = 4$ (12 minutes and 51 minutes slower, respectively). However, in the Chimney Walking and Wall Walking scenarios, RHCP with $\kappa_{\max} = 4$ remains faster than CVBFP on average (6.8 minutes and 50 minutes faster, respectively). When $\kappa_{\max} = 3$, RHCP is approximately 60 minutes faster than CVBFP in the Wall Walking scenario, while the comparison in the Chimney Climbing scenario depends on the component of the bimodal distribution. Component A (with a weighting of 0.75) is approximately 15 minutes faster than CVBFP, while the 95% HDI of component B partially intersects the ROPE, meaning it remains a credible possibility that no practical difference is present in this case.

The magnitudes of the planning time differences are very different between scenarios. For example, the greatest mean time saving in the Chimney Climbing scenario was only 2.9 minutes ($\kappa_{\max} = 1$, component A) compared to over an hour in the Wall Walking scenario ($\kappa_{\max} = 1$, component A). One explanation for this variation is the relative prevalence of CLM in different scenarios. For example,

CVBFP encountered at least one CLM in 97% of tests in the Wall Walking scenario, which may have contributed to significantly increasing its mean planning time, resulting in a large disparity between it and RHCP. By contrast, CVBFP encountered CLM in only 4% of tests in the Stepping Stones scenario, resulting in much closer comparisons between the two planners when $\kappa_{\max} \leq 3$.

Additionally, as the horizon depth increases, the planning time distributions typically become more consolidated into a single component. For example, in the Chimney Walking scenario, the weighting of component A is 0.55 when $\kappa_{\max} = 1$, increasing to 0.63 when $\kappa_{\max} = 2$ and 0.75 when $\kappa_{\max} = 3$, before becoming unimodal when $\kappa_{\max} = 4$. This is further demonstrated by the fact that the data for $\kappa_{\max} = 1$ is bimodal in all scenarios, while that for $\kappa_{\max} = 4$ is unimodal in all scenarios. This is likely because CLM occur less frequently for longer horizon depths.

8.2.2. Number of stance changes

Figure 31 shows that the number of stance changes also follows the expected pattern, with longer horizon depths generally corresponding to more efficient motion plans featuring fewer stance changes. However, this trend is somewhat occluded by the prevalence of bimodal distributions whose two components often have very different means. The relative prevalence of bimodality, as well as the large disparities between the two components, is likely due to CLM having a much greater impact on the number of stance changes made by RHCP than on the algorithm's planning time. This is to be expected, as the robot is often forced to retreat in the face of CLM, with the stance changes made during this retreat being counted towards this data. By contrast, the additional time needed to plan a retreat is often small, since the previous node can be restored from the global cache \mathcal{C}_G rather than being generated anew.

Figure 31 also shows that, in the Wall Walking scenario, RHCP with $\kappa_{\max} = 4$ generates motion plans requiring meaningfully fewer stance changes than CVBFP on average (48.8 fewer, 47%), while in the Chimney Climbing scenario the 95% HDI for this planning horizon is entirely contained within the ROPE, suggesting that the difference in path efficiency is not practically meaningful. In the Stepping Stones scenario, the distribution for RHCP with $\kappa_{\max} = 4$ is only partially contained by the ROPE, suggesting that the true difference may be a very modest decrease (6.4 stance changes) with respect to CVBFP, though the most likely case is that the true difference is not meaningful.

The Chimney walking scenario does not follow this trend, however. Here, the data for RHCP with $\kappa_{\max} = 4$ is bimodal, with only component A (weighted approximately 0.75) reflecting a meaningful improvement over CVBFP (17.9, or 23%, fewer stance changes on average).

Component B, on the other hand, reflects a very large increase (1050 additional changes on average, or 1344%).

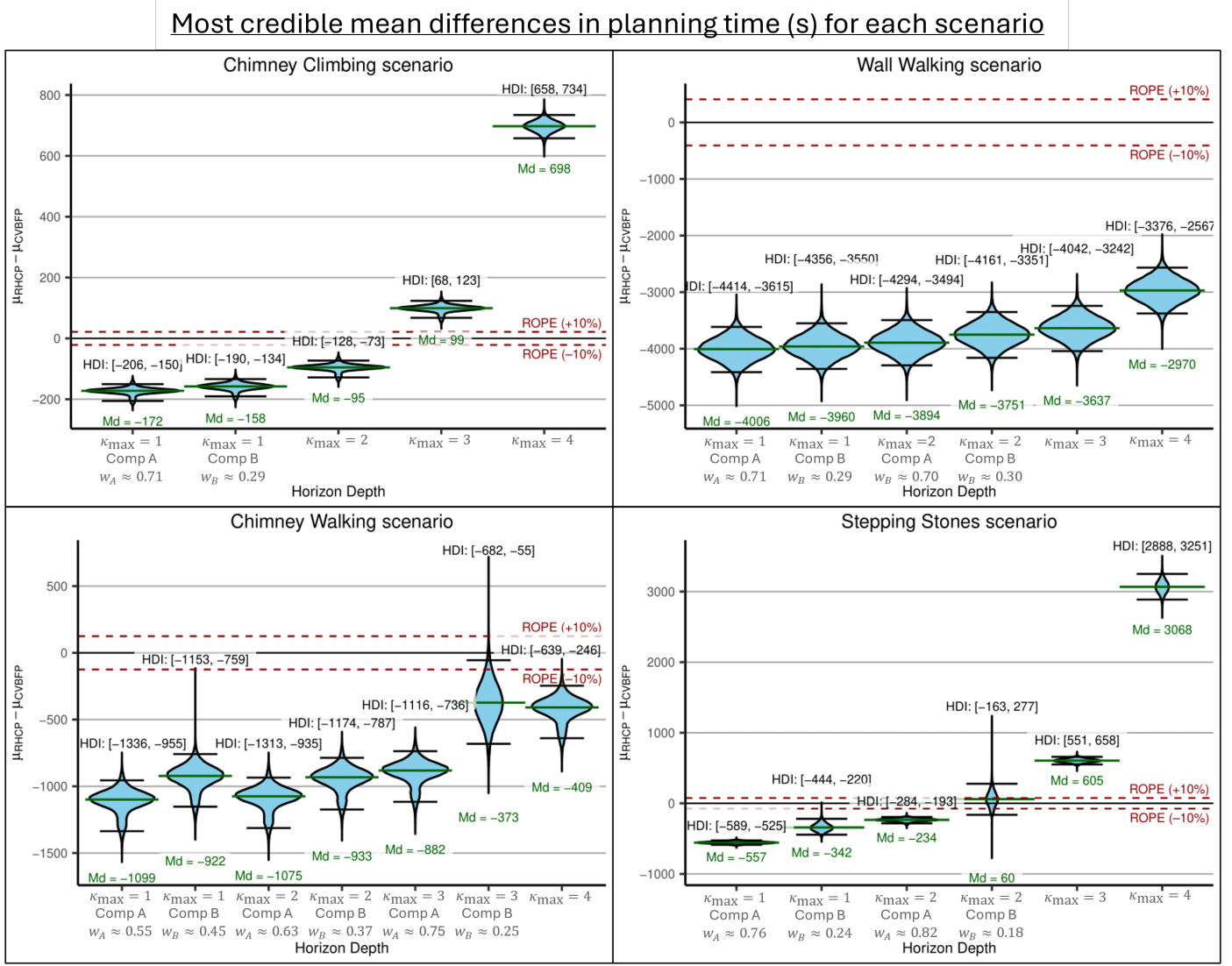


Figure 30: Probability distributions of the difference in planning times (s) between RHCP and CVBFP in each scenario. Each violin denotes a different value of κ_{\max} . Where the distribution for a given horizon depth is bimodal, the two components (A and B) are shown separately. The 95% HDI is marked on each violin by black horizontal bars, while the median is shown in green. The ROPE for each environment is shown as red dashed horizontal lines. Violins below the ROPE’s lowerbound favour RHCP in a statistically significant way. Conversely, violins above the ROPE’s upperbound favour CVBFP. When violins overlap with the ROPE, no strong conclusions can be drawn.

Indeed, the data for the Chimney Walking scenario shows a peculiar trend where the secondary components of each distribution exhibit larger numbers of stance changes as the horizon depth increases — the opposite of the trend seen elsewhere in this data. This is somewhat offset by the approximate value of w_B decreasing as the horizon depth increases. Taken together, these trends suggest that planning attempts in the Chimney Walking scenario with longer horizon depths are less likely to encounter a CLM, but the consequences of doing so become more dire.

This is believed to be caused by an unintended emergent behaviour of the CLM intervention mechanism, discussed in Section 6.2. The motion plans requiring the largest numbers of stance changes often involved the robot becoming trapped in a configuration resembling that

shown in Figure 32. From this configuration, if the robot lifts either of its rear feet, then it will become unable to lift the other without loss of balance, causing a CLM.

Ordinarily, the intervention mechanism would resolve the CLM by forcing the robot to retreat and pre-emptively lift the foot that is becoming trapped. However, in this case the heuristic worsens the problem because lifting the trapped foot causes *another* CLM in which the other rear foot is trapped. This then triggers the intervention mechanism again, causing *another* CLM, and so on. This loop continues, making a very large number of unnecessary stance changes, until the robot has occupied every node on the horizon from the perspective of that shown in Figure 32. At this point, the planner backs up to the parent node of that shown in Figure 32 and thence escapes from the trap-

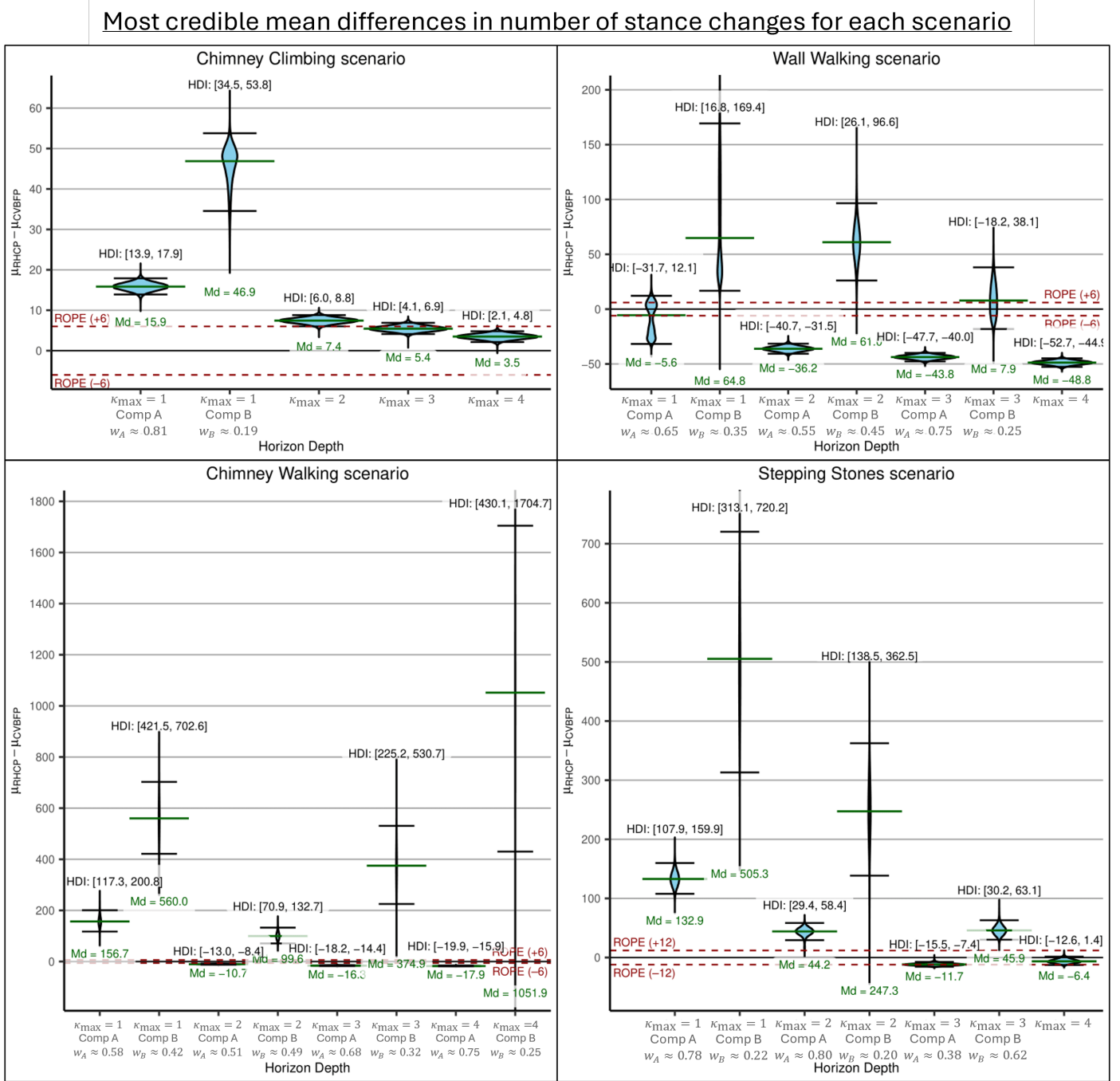


Figure 31: Probability distributions of the difference in stance changes between RHCP and CVBFP in each scenario, plotted according to the same conventions as Figure 30. The ROPE for each environment is shown as red dashed horizontal lines. Violins below the ROPE's lowerbound favour RHCP in a statistically significant way. Conversely, violins above the ROPE's upperbound favour CVBFP. When violins overlap with the ROPE, no strong conclusions can be drawn. When the HDI is completely inside the ROPE, both planners are considered to be statistically equivalent.

ping loop. RHCP variants with longer horizons are more severely affected by this problem because the number of nodes on the horizon from the perspective of Figure 32 grows exponentially with the horizon depth.

In summary, the general trend observed in Figures 30 and 31 is that short horizon depths (*i.e.*, $\kappa_{\max} \leq 2$) typically result in faster performance than CVBFP at the cost

of less efficient planning outputs. Likewise, longer horizon depths (*i.e.*, $\kappa_{\max} \geq 3$) typically correspond to paths of better or equivalent quality to those of CVBFP, while requiring more time to generate. In most scenarios, there is no value of κ_{\max} for which RHCP exceeds CVBFP in *both* metrics, with the exception of the Wall Walking scenario, in which this is true when $\kappa_{\max} = 4$.

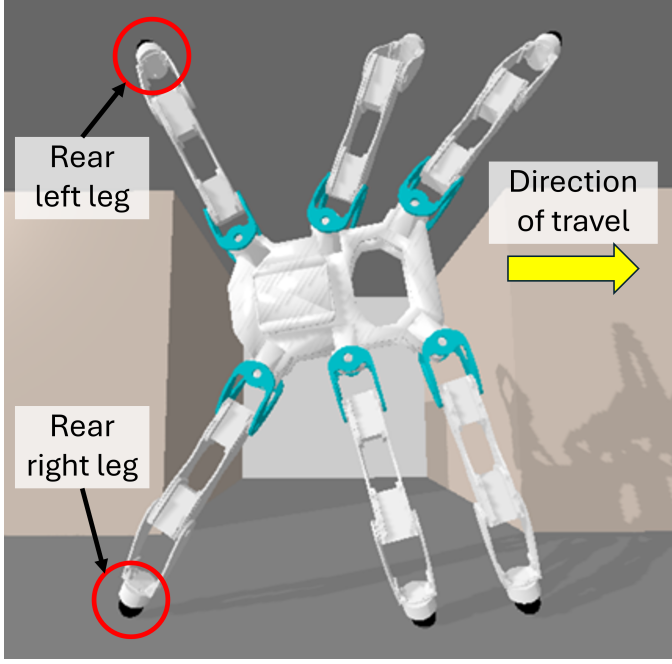


Figure 32: Image of the Corin hexapod in a configuration resulting in especially pernicious CLM behaviour.

9. Conclusions

This paper presented a novel multi-contact motion planning framework for legged robots, consisting of a receding-horizon tree search methodology and a posture generator utilising vector-field inequalities. The proposed motion planner (RHCP) successfully generated several motions for the hexapod robot Corin [13] in four challenging environments belonging to different classes: the Stepping Stones scenario requires the robot to walk over a ‘river’ using sparse and irregularly placed surfaces; the Wall Walking scenario features a narrow corridor that requires contacts to be formed on a vertical wall; the Chimney Walking scenario requires a large gap to be crossed using the vertical surfaces exclusively; and the Chimney Climbing scenario sees the robot vertically climb up a chimney. Our approach adds new capabilities not found in the state-of-the-art, including rapid re-planing capabilities, reduced susceptibility to contact-critical local minima, and simultaneously planning whole-body linking trajectories alongside the stance sequence.

A thorough experimental comparison of RHCP and CVBFP in virtual environments found that, with short horizon depths ($\kappa_{\max} \leq 2$), RHCP consistently generates plans as fast or faster than CVBFP across all scenarios tested, though these plans are generally of lower quality. Likewise, longer horizon depths ($\kappa_{\max} \geq 3$) typically result in motion plans that are as efficient or more efficient than those of CVBFP across all scenarios, while requiring more time to generate. The exception to this rule was the Wall Walking scenario, in which RHCP with $\kappa_{\max} = 4$ generated stance sequences that were more efficient than those

of CVBFP while also requiring less time to plan.

Though RHCP sacrifices CVBFP’s guarantee of completeness, we find experimentally that only one of our 1400 motion planning attempts using RHCP were affected by this.

The undesired emergent behaviours displayed by the heuristic intervention mechanism in some scenarios (most notably Chimney Walking) represents a major limitation of our current approach, as does the reliance on heuristics to mitigate CLM issues more generally. Therefore, a major focus of future work is to reformulate the posture generator such that contacts can be placed in such a way that CLM are prevented from forming. Another limitation of the approach is that it can be difficult to predict which horizon depth is most applicable for a given situation, which we plan to address through the development of an adaptive mechanism. Furthermore, the current formulation relies on a precise model of the environment using mathematical primitives such as planes. In order to support real-time planning operations in unknown environments, the planner will need to be reformulated in order to handle uncertainty in the environment model, and to work with partially observed scenarios. Finally, future work also aims to validate the motion plans presented here by executing them with a physical robot.

CRedit Authorship Contribution Statement

Daniel S. J. Derwent: Conceptualization, Methodology, Software, Validation, Formal analysis, Investigation, Data Curation, Writing - Original Draft, Visualization. **Simon Watson:** Conceptualization, Resources, Writing - Review & Editing, Supervision, Project administration. **Bruno V. Adorno:** Conceptualization, Methodology, Resources, Writing - Review & Editing, Supervision, Project administration, Funding acquisition.

Declaration of Competing Interest

The authors declare that they have no known competing financial interests or personal relationships that could have appeared to influence the work reported in this paper.

Acknowledgements

This work was supported by a grant from the University of Manchester and by the Royal Academy of Engineering under the Research Chairs and Senior Research Fellowships programme. Sponsoring organisations did not have any involvement in the study design, the collection, analysis or interpretation of data, the writing of this article or decision to submit this article for publication.

Corin was developed by Hassan Hakim Khalili and Wei Cheah [13]. R code used for statistical analysis in Section 8 was based on scripts released by John K. Kruschke, with adaptations by Ana Christina Almada Campos and the authors.

Data Availability

Research data related to this article is available through Figshare [26].

References

- [1] T. Bretl, Motion planning of multi-limbed robots subject to equilibrium constraints: The free-climbing robot problem, *The International Journal of Robotics Research* 25 (4) (2006) 317–342. doi:10.1177/0278364906063979.
- [2] K. Hauser, T. Bretl, K. Harada, J.-C. Latombe, Using Motion Primitives in Probabilistic Sample-Based Planning for Humanoid Robots, Springer Berlin Heidelberg, Berlin, Heidelberg, 2008, pp. 507–522. doi:10.1007/978-3-540-68405-3_32.
- [3] K. Hauser, T. Bretl, J.-C. Latombe, B. Wilcox, Motion Planning for a Six-Legged Lunar Robot, Springer Berlin Heidelberg, Berlin, Heidelberg, 2008, pp. 301–316. doi:10.1007/978-3-540-68405-3_19.
- [4] A. Escande, A. Kheddar, S. Miossec, Planning contact points for humanoid robots, *Robotics and Autonomous Systems* 61 (5) (2013) 428–442. doi:https://doi.org/10.1016/j.robot.2013.01.008.
- [5] P. Ferrari, L. Rossini, F. Ruscelli, A. Laurenzi, G. Oriolo, N. G. Tsagarakis, E. Mingo Hoffman, Multi-contact planning and control for humanoid robots: Design and validation of a complete framework, *Robotics and Autonomous Systems* 166 (2023) 104448. doi:https://doi.org/10.1016/j.robot.2023.104448.
- [6] S. Tonneau, A. Del Prete, J. Pettré, C. Park, D. Manocha, N. Mansard, An efficient acyclic contact planner for multiped robots, *IEEE Transactions on Robotics* 34 (3) (2018) 586–601. doi:10.1109/TRO.2018.2819658.
- [7] K. Hauser, T. Bretl, J.-C. Latombe, Non-gaited humanoid locomotion planning, in: 5th IEEE-RAS International Conference on Humanoid Robots, 2005., 2005, pp. 7–12. doi:10.1109/ICHR.2005.1573537.
- [8] I. Mordatch, E. Todorov, Z. Popović, Discovery of complex behaviors through contact-invariant optimization, *ACM Transactions on Graphics* 31 (4) (Jul. 2012). doi:10.1145/2185520.2185539.
- [9] M. Kalakrishnan, J. Buchli, P. Pastor, M. Mistry, S. Schaal, Learning, planning, and control for quadruped locomotion over challenging terrain, *The International Journal of Robotics Research* 30 (2) (2011) 236–258. doi:10.1177/0278364910388677.
- [10] J. Wang, T. S. Lembono, S. Kim, S. Calinon, S. Vi-jayakumar, S. Tonneau, Learning to guide online multi-contact receding horizon planning, in: 2022 IEEE/RSJ International Conference on Intelligent Robots and Systems (IROS), 2022, pp. 12942–12949. doi:10.1109/IROS47612.2022.9981234.
- [11] O. Melon, R. Orsolino, D. Surovik, M. Geisert, I. Havoutis, M. Fallon, Receding-horizon perceptive trajectory optimization for dynamic legged locomotion with learned initialization, in: 2021 IEEE International Conference on Robotics and Automation (ICRA), 2021, pp. 9805–9811. doi:10.1109/ICRA48506.2021.9560794.
- [12] A. W. Winkler, C. D. Bellicoso, M. Hutter, J. Buchli, Gait and trajectory optimization for legged systems through phase-based end-effector parameterization, *IEEE Robotics and Automation Letters* 3 (3) (2018) 1560–1567. doi:10.1109/LRA.2018.2798285.
- [13] University of Manchester, Corin, accessed: Jan. 29, 2026 (2020). URL <https://uomrobotics.com/robots/corin.html>
- [14] D. S. J. Derwent, S. Watson, B. V. Adorno, Multi-contact posture generation using vector field inequalities, in: A. Cavalcanti, S. Foster, R. Richardson (Eds.), *Towards Autonomous Robotic Systems*, Springer Nature Switzerland, Cham, 2026, pp. 111–123. doi:10.1007/978-3-032-01486-3_10.
- [15] B. Vilhena Adorno, Robot Kinematic Modeling and Control Based on Dual Quaternion Algebra — Part I: Fundamentals., working paper or preprint (Feb. 2017). URL <https://hal.science/hal-01478225>
- [16] M. M. Marinho, B. V. Adorno, K. Harada, M. Mitsuishi, Dynamic active constraints for surgical robots using vector-field inequalities, *IEEE Transactions on Robotics* 35 (5) (2019) 1166–1185. doi:10.1109/TRO.2019.2920078.
- [17] M. S. Pereira, B. V. Adorno, Manipulation Task Planning and Motion Control Using Task Relaxations, *Journal of Control, Automation and Electrical Systems* 33 (4) (2022) 1103–1115, publisher: Springer US. doi:10.1007/s40313-022-00915-0.
- [18] J. J. Quiroz-Omaña, B. V. Adorno, Whole-body control with (self) collision avoidance using vector field inequalities, *IEEE Robotics and Automation Letters* 4 (4) (2019) 4048–4053. doi:10.1109/LRA.2019.2928783.
- [19] K. Bouyarmane, A. Escande, F. Lamiriaux, A. Kheddar, Potential field guide for humanoid multicontacts acyclic motion planning, in: 2009 IEEE International Conference on Robotics and Automation, 2009, pp. 1165–1170. doi:10.1109/ROBOT.2009.5152353.

- [20] T. Bretl, S. Lall, Testing static equilibrium for legged robots, *IEEE Transactions on Robotics* 24 (4) (2008) 794–807. doi:10.1109/TRO.2008.2001360.
- [21] I. Kao, K. Lynch, J. W. Burdick, *Contact Modeling and Manipulation*, Springer Berlin Heidelberg, Berlin, Heidelberg, 2008, pp. 647–669. doi:10.1007/978-3-540-30301-5_28.
- [22] B. V. Adorno, M. M. Marinho, Dq robotics: A library for robot modeling and control, *IEEE Robotics & Automation Magazine* 28 (3) (2021) 102–116. doi:10.1109/MRA.2020.2997920.
- [23] Erwin Coumans, Bullet physics, version 3.25, Released: Apr. 25, 2022.
URL <http://bulletphysics.org>
- [24] J. K. Kruschke, Bayesian estimation supersedes the t test., *Journal of experimental psychology: General* 142 (2) (2013) 573. doi:10.1037/a0029146.
- [25] Student, The probable error of a mean, *Biometrika* 6 (1) (1908) 1–25. doi:10.2307/2331554.
- [26] D. Johnson, B. Adorno, S. Watson, RHCP Comparison Dataset Jan26 (Jan 2026). doi:10.48420/31189942.